CONTRACTOR REPORT

SAND87—7036
Unlimited Release
UC—721

Mineralogy of the Rustler Formation in the WIPP-19 Core

Terry Sewards, Rosemary Glenn, Klaus Keil
Department of Geology and Institute of Meteoritics
University of New Mexico
Albuquerque, NM 87131

Prepared by Sandia National Laboratories Albuquerque, New Mexico 87185 and Livermore, California 94550 for the United States Department of Energy under Contract DE-AC04-76DP00789

Printed March 1991

Issued by Sandia National Laboratories, operated for the United States Department of Energy by Sandia Corporation.

Available to DOE and DOE contractors from
Office of Scientific and Technical Information
PO Box 62
Oak Ridge, TN 37831

Prices available from (615) 576-8401, FTS 626-8401

Available to the public from
National Technical Information Service
US Department of Commerce
5285 Port Royal Rd
Springfield, VA 22161

NTIS price codes
Printed copy: A05
Microfiche copy: A01

SAND87-7036
Unlimited Release
Printed March 1991

Distribution
Category UC-721

MINERALOGY OF THE RUSTLER FORMATION IN THE WIPP-19 CORE*

Terry Sewards, Rosemary Glenn, and Klaus Keil

Department of Geology and Institute of Meteoritics
University of New Mexico, Albuquerque, NM 87131

ABSTRACT

The mineralogy of the Rustler Formation is a critical element in many of the radionuclide release models for the Waste Isolation Pilot Plant (WIPP), and it is necessary to know the abundances of the various minerals present, their compositions, their textures and locations with respect to water-bearing features, and their interrelationships. Clay mineralogy in particular is of vital importance because of the ability of clay minerals to sorb contaminant cations. Furthermore, the minerals present in the different units of the Rustler Formation are possible sources for solutes present in waters taken from various boreholes in the vicinity of the WIPP site.

This report characterizes the mineralogy of the Rustler Formation as represented in core from borehole WIPP-19. The major components, as determined by x-ray diffraction (XRD), are halite, anhydrite, gypsum, dolomite, magnesite, quartz, and clay. Minor components include calcite, pyrite, feldspar and phyllosilicates of metamorphic origin (muscovite, biotite, and chlorite). Clay minerals, identified by XRD, include illite, serpentine, chlorite, and mixed-layer chlorite/smectite (including corrensite).

Quartz and clay, with some halite and anhydrite, dominate the lower member; the Culebra and Magenta units are primarily dolomite with some quartz and clay, while the Forty-niner Member consists of quartz, clay, and sulfates (anhydrite and gypsum).

Halite occurs in four textural styles: bedded, recrystallized halite; displacive halite; as a cement in mud/siltstones; and as a fracture-filling, and is largely restricted to the lower member. Anhydrite occurs primarily as a massive, crudely banded nodular structure, although there is often evidence of partial alteration to gypsum. Gypsum also is usually massive, in a crudely banded form. The massive areas consist of fine-grained

*The work described in this report was performed for Sandia National Laboratories under Contracts No. 01-6328 and 32-6811.

irregular crystals ("patchy" gypsum); these areas are separated by veins of "fibrous" gypsum, usually parallel to bedding. Fibrous gypsum vein filling in other lithologies is very common. Dolomite is unfossiliferous, laminated, and very fine-grained; it contains numerous vugs and fractures: these are usually lined with clay, gypsum, and powdery dolomite. Magnesite, a relatively minor component, occurs as microcrystalline nodules and as euhedral elongated platy crystals included in halite. Quartz and clay always occur together with minor amounts of feldspar and detrital phyllosilicate grains. Calcite is restricted to a thin bed above the Culebra Dolomite in the samples studied.

In general, this study should be considered a detailed analysis of the Rustler section mineralogy. It is unlikely that any other minerals are present elsewhere in the Rustler Formation in any great quantity. Abundances of individual minerals may vary considerably in other areas of the formation.

ACKNOWLEDGMENT

Dr. D. G. Brookins of the University of New Mexico reviewed this report and provided invaluable assistance in preparing materials used in the text, figures, and tables.

The authors also acknowledge the contributions made by several scientists from Sandia National Laboratories. C. L. Stein provided guidance in the initial stages of this work and assisted the authors in the collection of the samples examined in this report. The detailed critical reviews of early versions of this manuscript by S. J. Lambert and K. L. Robinson led to significant improvements in the report. Additional reviews by J. Krumhansl were also helpful. M. D. Siegel was responsible for the preparation of final draft of the report and coordinated technical and management reviews.

CONTENTS

FIGURES

TABLES

I. INTRODUCTION

The Rustler Formation, which overlies the Salado Formation in the Delaware Basin, into which the Waste Isolation Pilot Plant (WIPP) repository has been excavated, contains several brittle lithologic units, which are extensively fractured due to dissolution of halite in the upper Salado Formation and in the lower unit of the Rustler Formation itself (Ferrall and Gibbons, 1979; Lambert, 1983). These units, particularly the Culebra and Magenta Dolomite members, have field-measurable fracture porosities and have significant amounts of water moving through them. In order to evaluate the consequences of a low-pressure hydrologic breach of the WIPP facility, it is necessary to model the regional transport of radionuclides within the Rustler Formation. The mineralogy of the Rustler Formation is a critical element in any such model: it is necessary to know the abundances of the various minerals present, their compositions, their textures and locations with respect to water-bearing fractures, and their interrelationships. Clay mineralogy in particular is of vital importance, because of the ability of clay minerals to sorb contaminant cations. Furthermore, the minerals present in the different units of the Rustler Formation are possible sources for solutes present in waters taken from various boreholes in the vicinity of the WIPP site.

The objective of this report is, therefore, to characterize the mineralogy of the Rustler Formation as seen in 1 core (WIPP-19) in as much detail as possible, so that this information may be used in subsequent studies, particularly hydrological models, of the region. One basic limitation of the study is the fact that only 1 core was examined; lateral variations in the mineralogy are not documented here, although they are obviously present (Ferrall and Gibbons, 1979). To a certain extent, this deficiency has been overcome by a detailed study of the Culebra Dolomite unit from eight boreholes (Sewards et al., 1991).

II. GENERAL SITE GEOLOGY

Regional Geologic Setting

The Upper Permian (Ochoan) Rustler Formation is part of a sequence of evaporite and clastic rock units deposited in the Delaware, Midland, Palo Duro, and Dalhart Basins in southeastern New Mexico and western Texas (Figure II-1). In the latter 2 basins, it is known as the Alibates Formation (McGillis and Presley, 1981). In the Delaware Basin (Figure II-2), which is ringed by the Capitan Reef Complex, the Rustler Formation overlies the Salado Formation, which is composed mainly of thick halite beds, mud/sandstones, abundant anhydrite, and a suite of potash salts. The Rustler, in turn, is overlain by the Dewey Lake Red Beds, composed almost entirely of mud/siltstone, which may represent the final regression of the Permian seas from the Delaware and related basins (Figure II-3).

Stratigraphy and Lithology

The core study of the Rustler Formation completed by Ferrall and Gibbons (1979) includes a lithologic log for the WIPP-19 borehole. A modification of this log is included here (Figure II-4). In this log, the Rustler Formation is divided into 5 members: within each member, except the Culebra and Magenta Dolomites, there are several individual lithologic units.

The (unnamed) lower member, which can be described as a mud/siltstone complex with occasional interbedded, generally argillaceous halite, begins with a reddish mudstone (mudstone 1 - first solution residue, 894 to 892 ft) (271 to 270 m) in contact with the uppermost Salado Formation. This grades into a grey mud/siltstone (mudstone 2, 892 to 840 ft) (270 to 255 m) which is cemented with halite and mixed with coarse halite grains and retains primary depositional features (horizontal lamination, etc.). The grey mud/siltstone grades into a reddish, muddy sandstone (second solution residue, 835 to 828 ft) (253 to 251 m). In this sandstone unit, halite increases in abundance over several feet until a chaotic mudstone/halite texture is apparent. Eventually, halite becomes predominant and displays a bedded texture with clay along bed boundaries (argillaceous halite, 828 to 815 ft) (251 to 247 m). A 3 ft interval of clean halite occurs at about 815 ft (247 m), overlain by a 2 ft thick anhydrite bed (812 to 810 ft) (246 to 245 m). Argillaceous halite with a chaotic texture occurs for another 10 ft (3.3 m) (810 to 800 ft) (245 to 242 m). This halite is overlain by a thin (2 ft) mud/siltstone (mudstone 3, third solution residue). An 11 ft bedded anhydrite overlies the mud/siltstone (798 to 787 ft) (242 to 238 m), followed by another reddish mudstone (787 to 778 ft, 238 to 236 m, mudstone 4, fourth solution residue). A 1 ft thick layer of black shale with dolomite cement is followed by the

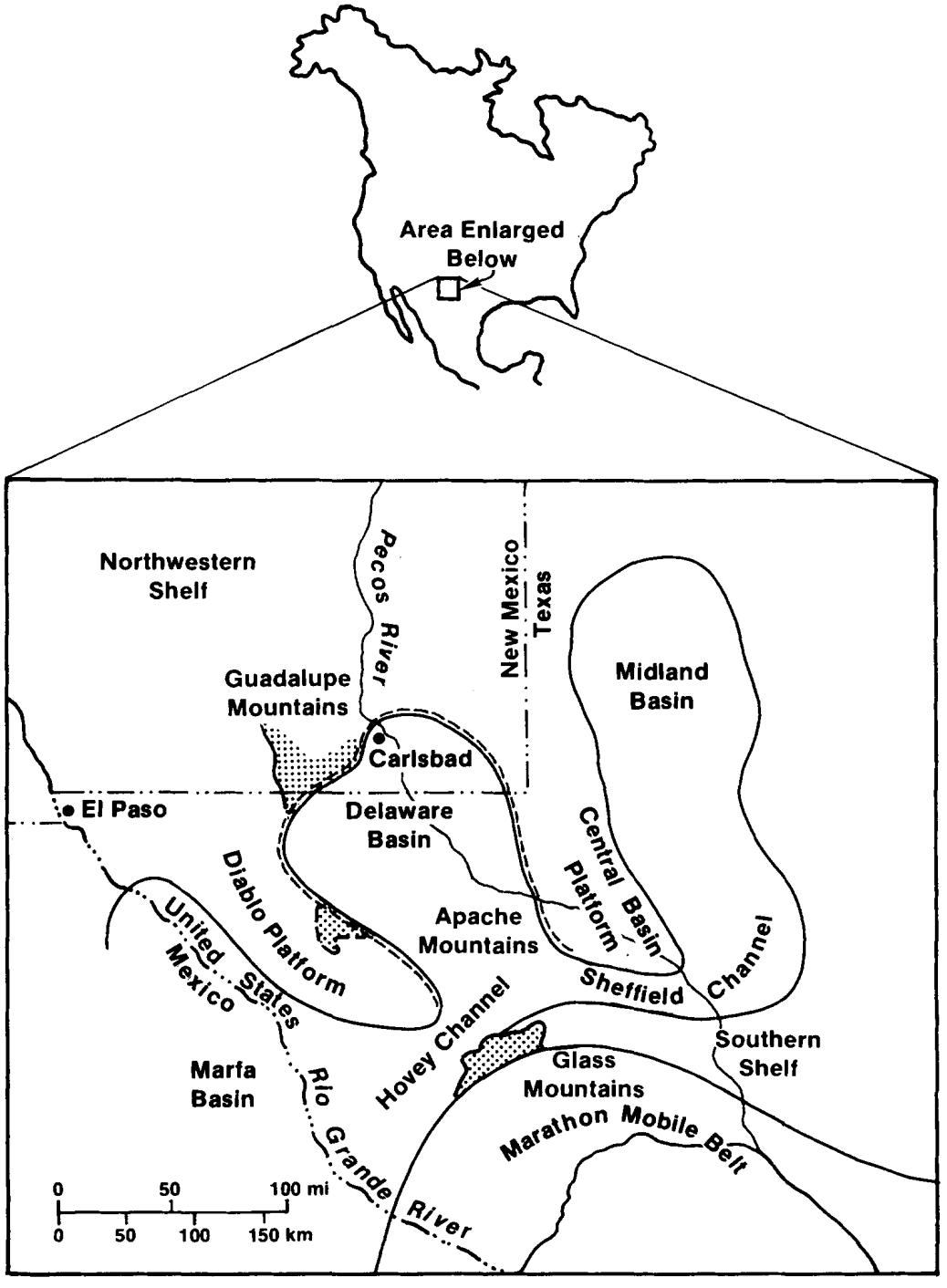

TRI-6342-472-0

Figure II-1. Permian Basin Paleogeography (modified after King, 1942).

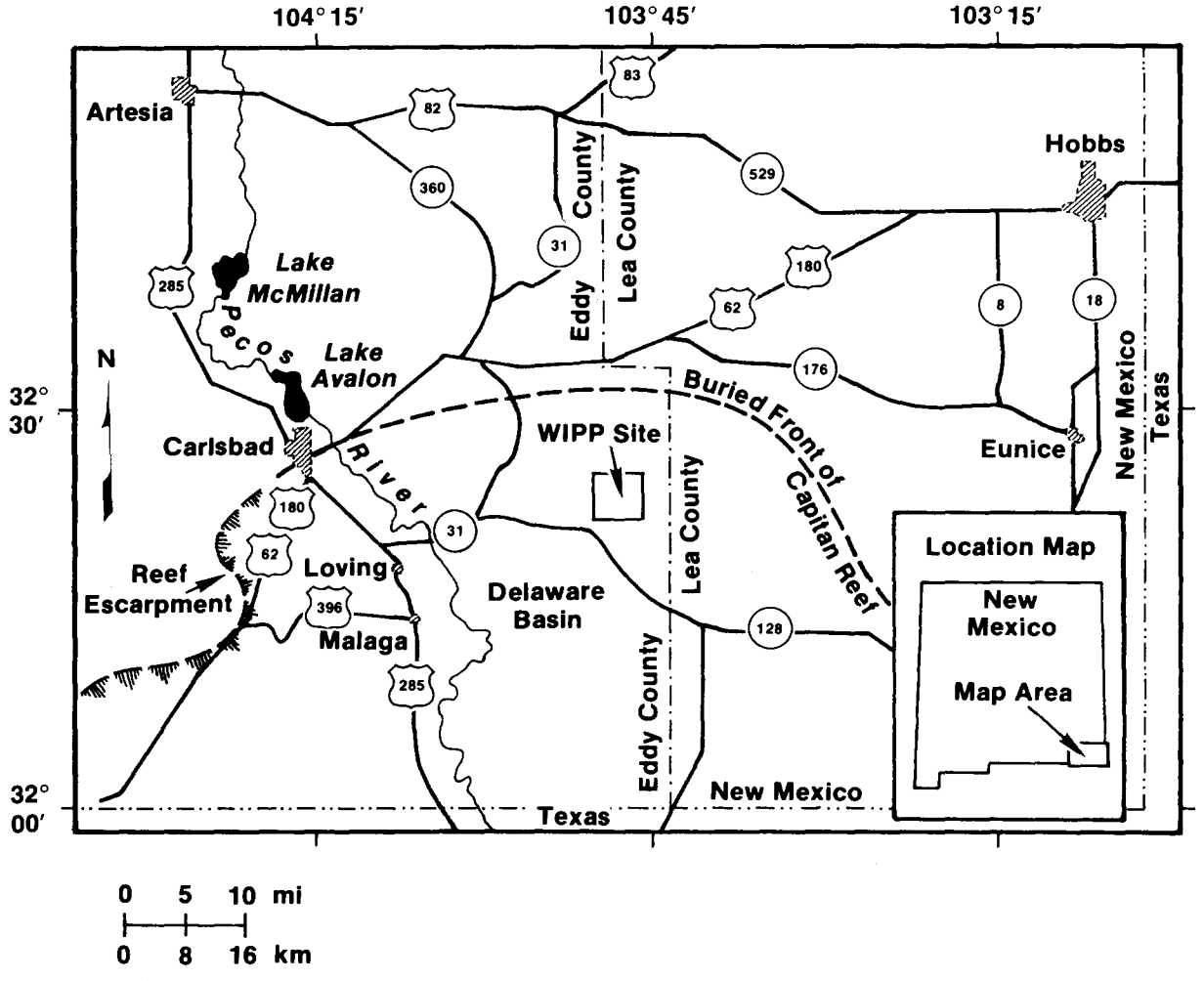

TRI-6342-528-0

Figure II-2. Regional Setting, Delaware Basin, Southeastern New Mexico (from Borns et al., 1983).

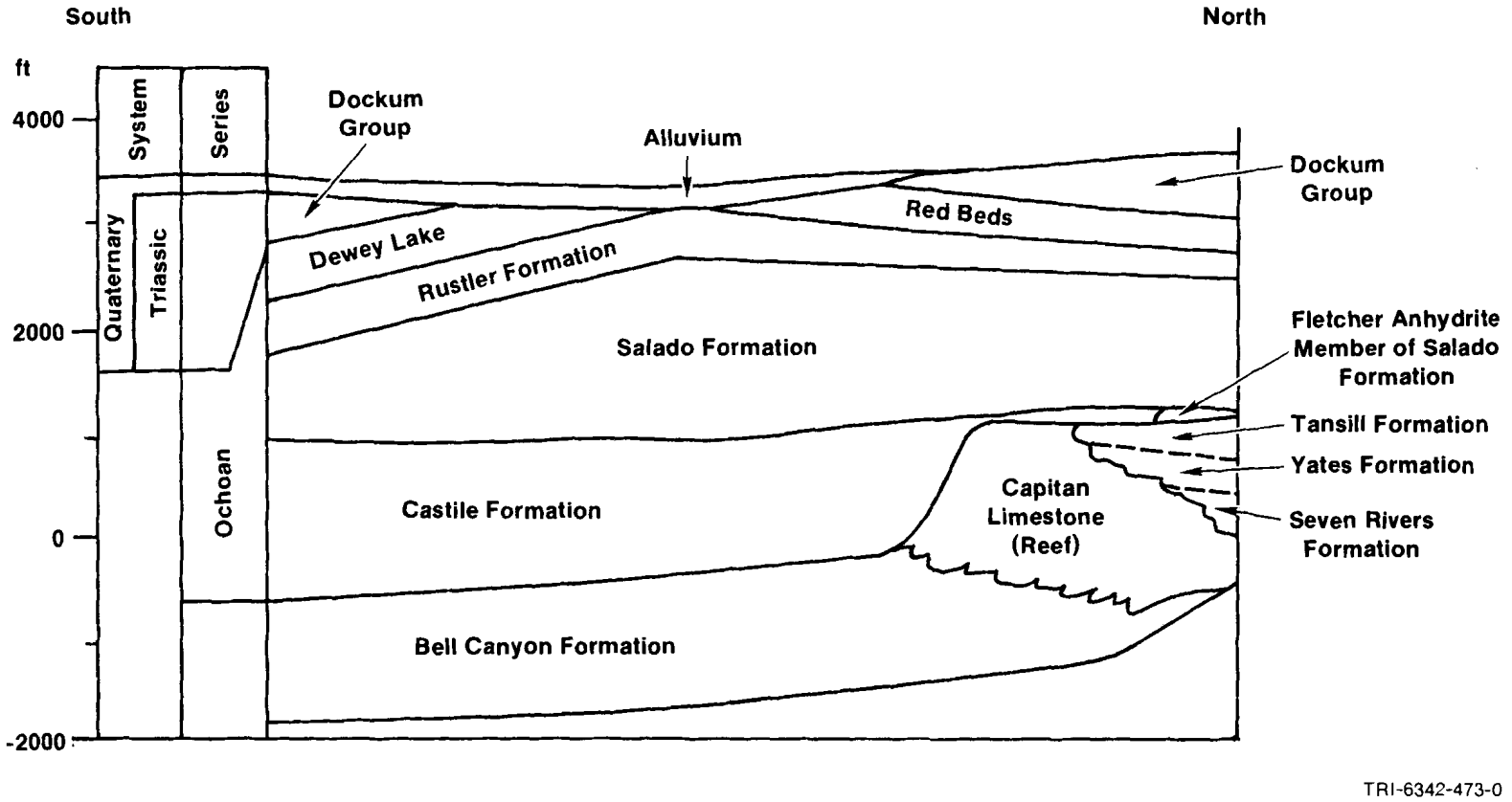

Figure II-3. Generalized North-South Cross Section, Delaware Basin, Southeastern New Mexico (modified from Borns et al., 1983).

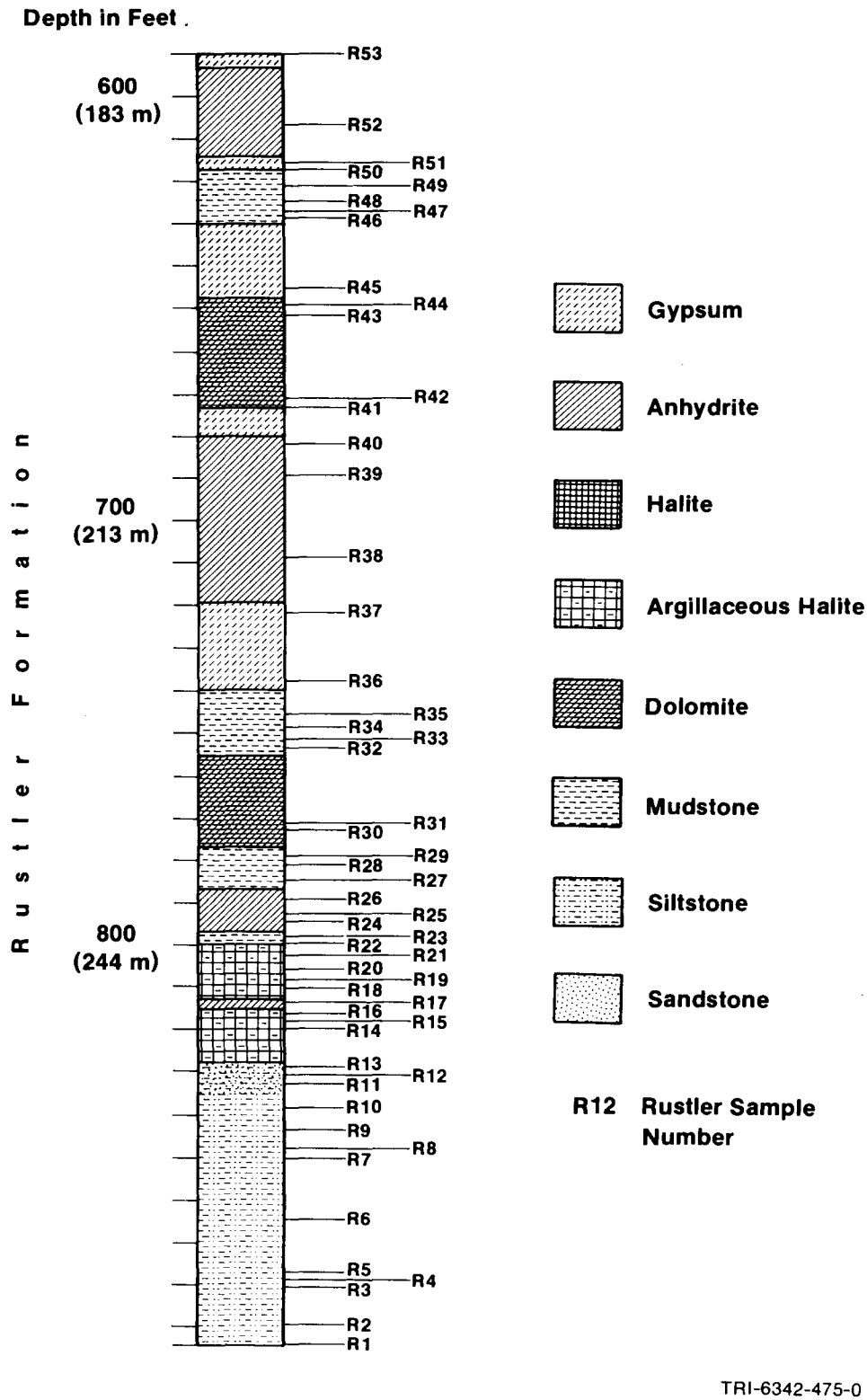

Figure II-4. Lithologic Log of WIPP-19 Core, Rustler Formation (modified from Ferrall and Gibbons, 1979).

Culebra Dolomite member (777 to 755 ft) (235 to 239 m), a fine-grained dolomite with abundant vugs and fractures, many of which are open. In the WIPP-19 core, the Culebra member is overlain by a thin (<1 ft) (.33 m) layer of calcite, followed by red-brown mud/siltstone (756 to 740 ft, 229 to 224 m, mudstone 5, fifth solution residue), followed by a 20 ft layer of gypsum, which has replaced anhydrite (740 to 720 ft) (224 to 218 m), a 20 ft thick bed of anhydrite (720 to 680 feet) (218 to 206 m), and a 7 ft layer (680 to 673 ft) (206 to 204 m) of gypsum after anhydrite. These sulfate units are overlain by the Magenta Dolomite member (673 to 648 ft) (204 to 196 m). Gypsum (after anhydrite, 648 to 630 ft) (196 to 191 m) overlies the dolomite, followed by mudstone 6 (sixth solution residue). The final 3 units are sulfates: a 2 ft thick anhydrite underlies a bed of laminated anhydrite (615 to 592 ft) (186 to 179 m), which is capped by a thin gypsum layer, which is in contact with the Dewey Lake Red Beds.

It should be emphasized here that the WIPP-19 core does not represent the complete Rustler Formation in the region surrounding the WIPP facility. For example, eastward of WIPP-19, halite occurs in the Tamarisk and Forty-niner members; westward there is no halite at all in the Rustler section.

Discussion

The Rustler section, although complicated when viewed in fine detail (Figure II-4), represents a fairly typical series of cycles of evaporite deposition, punctuated by episodes of high clastic input and dissolution. A simplified section (Figure II-5) shows the normal reverse salinity cycle of chloride facies (C) through sulfate facies (B) to carbonate facies (A), followed by a cycle of increasing salinity to the sulfate facies (B), a return to the carbonate facies (A), and a final increase in salinity to the sulfate facies (B). If mudstone 6 represents a halite solution residue, then the final cycle is more complete than is now apparent (ABC instead of AB).

Mudstone 2, a dark grey mud/siltstone with primary depositional sedimentary features, parallel lamination, and ripple lamination, has displacive halite and halite cement throughout the unit and was probably deposited while the basin brines were at halite saturation. Thus, the lower part of the Rustler section is, in fact, a continuation of a high salinity cycle, which originated in the Salado Formation. The division between the two formations is not so much due to a change in the nature of evaporite deposition, but rather to a drastic change in the rate of input of clastic material into the Delaware Basin.

The cause for the abrupt change in the amount of clastic input may have been a rise in the sediment level around the Capitan Reef and/or a subsidence of the basin and reef complex, which allowed new sources of detritus-bearing fresh water to penetrate the reef into the basin area.

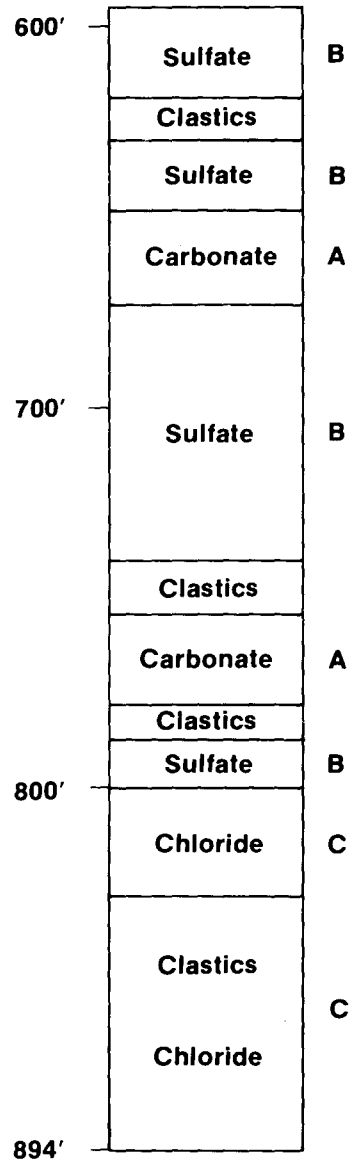

TRI-6342-484-0

Figure II-5. Simplified Stratigraphic Column of Rustler Section.

III. PROJECT SAMPLES

Rock samples used in this study were taken from the drill core of WIPP-19, the closest borehole to the WIPP repository with a complete section of the Rustler Formation (Figure III-1). WIPP-19 has a fairly complete section of the Rustler Formation; however, there are intervals from which no core was retrieved. Although the core was drilled using only salt-based mud and immediately cleaned to remove this material, the core was slabbed using kerosene. Every attempt was made to remove the kerosene-contaminated residue by scraping away the affected portions of the samples. It is assumed here that the compositions of minerals in the samples were not affected by the kerosene. It cannot, however, be assumed that mineralogical modes were not affected by salty residues of drilling brines.

Core samples for this study consisted of 52 portions from the WIPP-19 core. Samples ranged from 5 to 12 cm (2 to 4.7 in.) in length and were either 0.50 or 0.25 sections of the 4 in. (10 cm) drill core.

Selection Criteria

Samples were chosen by visual inspection to provide several types of information. First, an attempt was made to represent all major lithologic units in the formation, including mud/siltstones, carbonates, sulfates, and halite. Second, additional samples of mud/siltstones were taken to provide as much information as possible about the clay-bearing units, such as textural differences (clay seams, mud matrix, laminated mudstones versus massive, homogeneous regions) or color changes (grey, brown, red, green). Third, lithologic boundaries such as gradational or sharp contact and near contact regions were sampled in order to allow analysis of potential solution features and depositional changes.

Stratigraphic Location of Individual Samples

Figure III-2 shows the sample numbers and locations within the core.

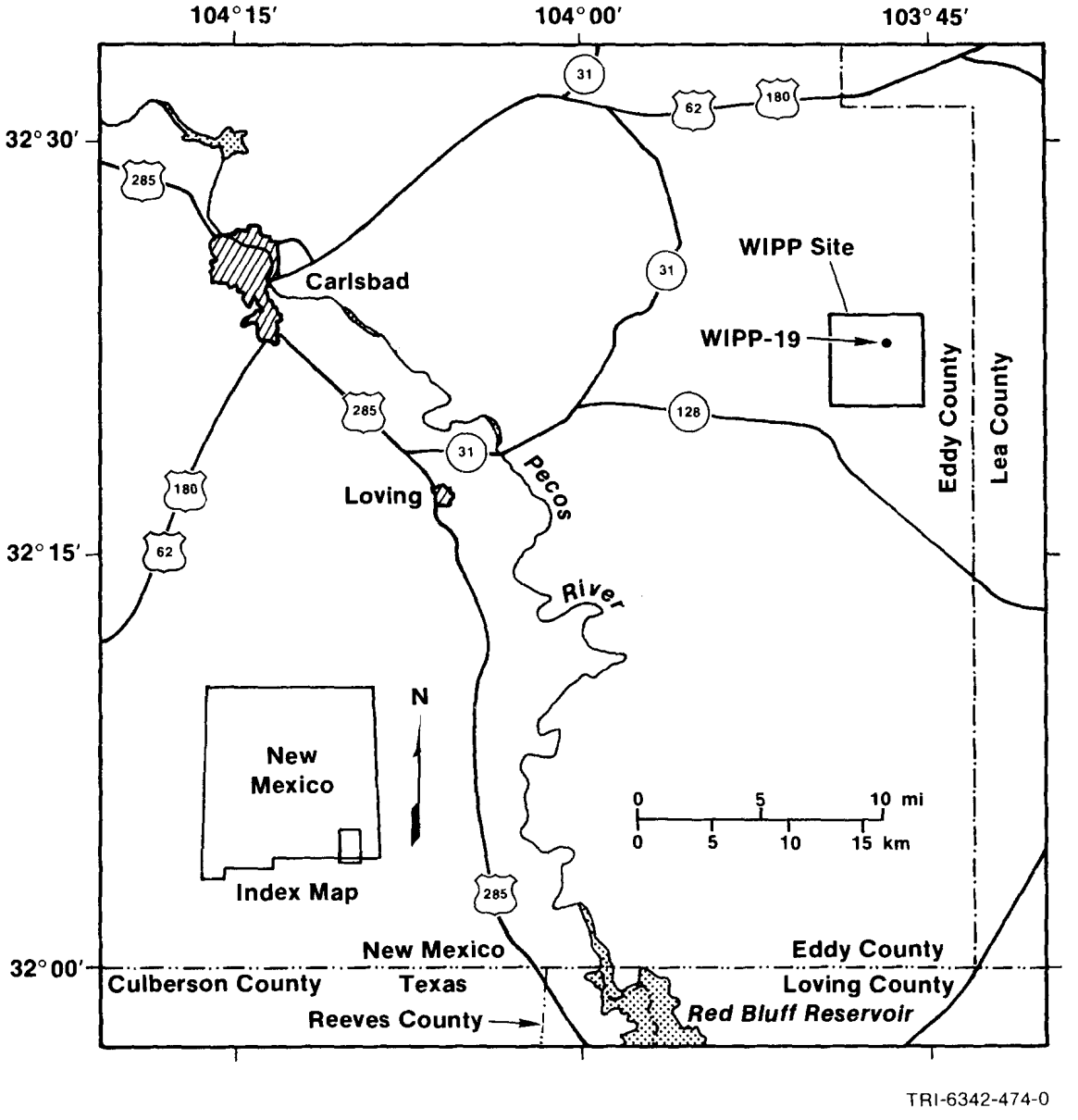

Figure III-1. Map Showing Location of Borehole WIPP-19.

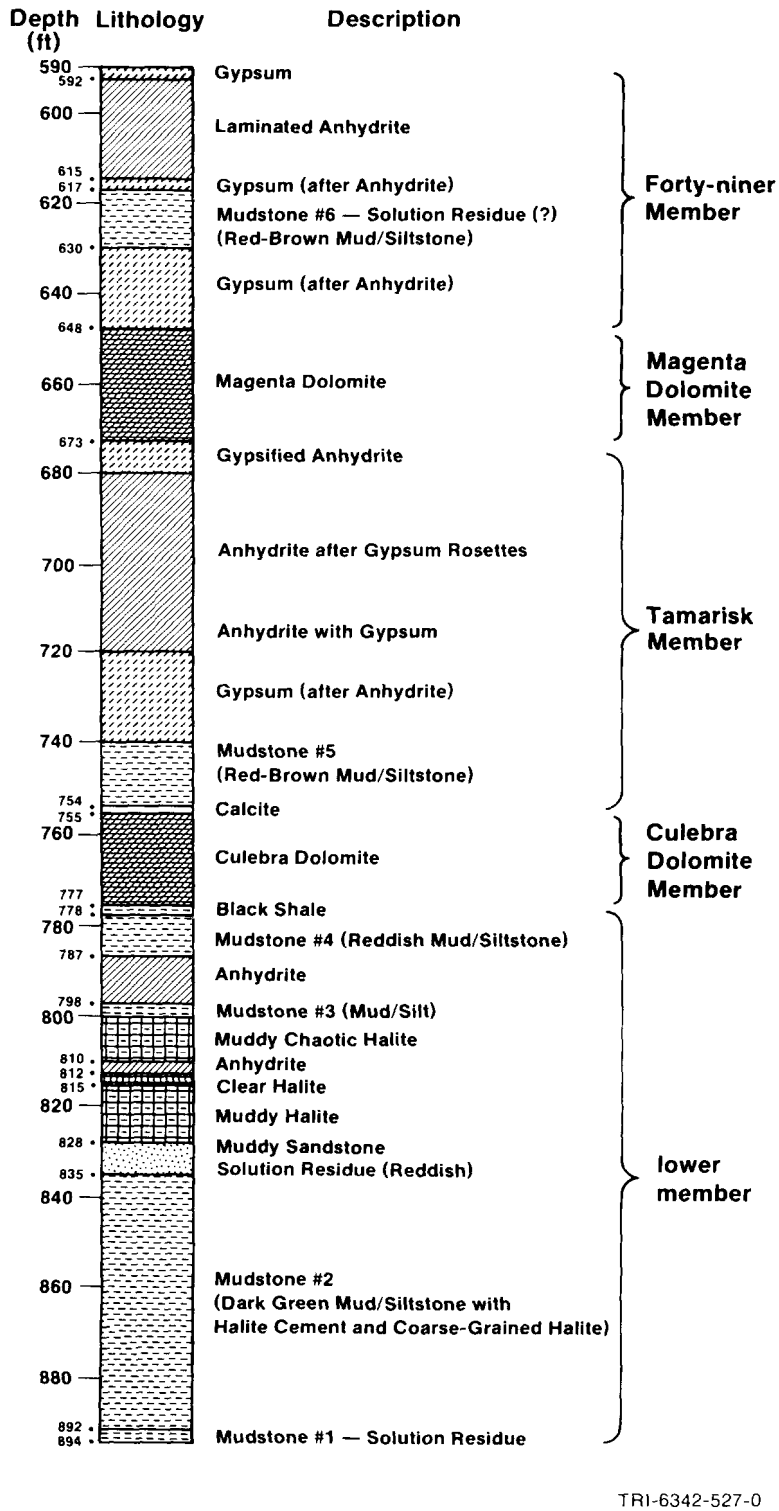

Figure III-2. Sample Locations, WIPP-19 Core.

IV. WHOLE ROCK COMPOSITIONAL DATA

All 52 samples were analyzed for their major element components by three methods. Twenty-four samples were ground up and dissolved in water to determine the amount of halite present, assumed to be equivalent to the mass loss during dissolution. The insoluble residue was then analyzed by x-ray fluorescence (XRF) for the remaining elements. Atomic absorption spectroscopy, in conjunction with wet chemistry, was used to analyze six samples: R2, R4, R6, R22, R33, and R43. The remaining samples were analyzed directly by XRF. Appendix A includes a description of the analytical methods used.

Summary of Compositional Data

The complete set of compositional data is listed in Table IV-1. This includes the NaCl data determined by dissolution. Figure IV-1 shows four major elements: Si, Mg, Ca, and S plus NaCl plotted against the depth for each sample. A stratigraphic column is included for reference.

Discussion

The accuracy of the values in Table IV-1 can be assessed qualitatively by inspection of the totals (except for samples R16 and R17, where NaCl was determined by difference). Using the modal mineralogical computation, one may ascribe water and carbon dioxide contents to the clay, gypsum, and carbonate components and add these amounts to the measured totals. If an average of 12% water content is ascribed to the clay, 20.9% water content for gypsum, and 47.7%, 57.2% and 44% CO_2 water contents for dolomite, magnesite, and calcite respectively, and if these amounts are added to the totals obtained by chemical analysis, the results come to within 7% of 100%, except for those samples with high anhydrite contents. This is apparently due to the fact that a gypsum standard was used for those samples with high calcium and sulfur, and matrix effects resulting from the structural difference between gypsum and anhydrite cause the concentrations of these elements to be underrepresented. Overall, with the exception of calcium and sulfur in the samples with high anhydrite modes, the accuracy of the individual oxides is probably around 10% of the amount present. It is also expected that the lower the amount of a particular oxide component is in a sample, the lower the accuracy will be for that element.

The graphic display of compositional data (Figure IV-1) shows a marked distinction between periods of high clastic input, which are presumably also periods of high freshwater input, and those of marine water dominated

Table IV-1. Major Element Compositions

Sample ID	Depth ft/m	SiO_2	Al_2O_3	MgO	FeO	CaO	K_2O	Na_2O	TiO_2	MnO	NaCl	SO_3	Total	H_2O+CO_2
R1	893.40/270.73	39.55	7.36	5.51	2.65	8.23	1.60	0.10	0.24	0.01	16.94	11.63	93.82	6.18
R2	891.20/270.06	50.52	6.95	7.58	1.82	6.00	3.20	1.30	0.30	0.03	10.39	7.87	95.96	4.04
R3	881.00/266.97	57.11	9.47	10.04	3.49	0.01	4.01	0.09	0.45	0.06	10.41	1.34	96.49	3.51
R4	880.20/266.73	53.60	8.76	10.63	2.89	0.54	3.48	0.00	0.36	0.05	5.08	0.95	86.34	13.66
R5	878.15/266.11	55.11	8.07	4.24	2.02	0.00	3.54	0.00	0.37	0.02	16.41	0.00	89.77	10.23
R6	867.40/262.85	53.60	8.85	7.66	2.25	3.85	3.80	0.00	0.43	0.03	12.70	0.74	93.91	6.09
R7	851.95/258.17	48.50	7.03	3.91	1.84	2.91	3.63	0.12	0.36	0.02	19.72	1.16	89.20	10.80
R8	850.75/257.80	50.31	6.31	3.45	1.95	3.28	3.11	0.00	0.23	0.02	19.03	2.50	90.17	9.83
R9	843.80/255.70	44.79	8.16	4.96	2.33	0.00	3.32	0.08	0.42	0.03	25.76	1.12	90.96	9.04
R10	839.20/254.30	47.35	5.87	3.78	2.35	3.10	2.68	0.00	0.25	0.02	16.16	2.33	83.88	16.12
R11	835.45/253.17	45.54	5.99	4.61	2.36	6.51	2.85	0.00	0.27	0.02	12.54	3.07	83.75	16.25
R12	832.65/252.32	42.66	5.15	2.82	1.59	6.52	2.78	0.14	0.19	0.01	18.37	8.34	88.56	11.44
R13	828.70/251.12	43.00	4.87	2.21	2.05	1.39	1.97	0.00	0.19	0.01	30.85	2.31	88.86	11.14
R14	819.25/248.26	42.45	4.89	2.99	2.29	1.33	1.41	0.00	0.30	0.02	27.40	2.79	85.88	14.12
R15	816.75/247.50	40.73	5.07	4.68	2.55	4.68	1.64	0.00	0.23	0.02	24.78	6.79	91.16	8.84
R16	814.65/246.86	0.21	0.07	0.07	0.00	0.22	0.00	0.00	0.00	0.00	98.49	0.94	100.00	0.00
R17	812.90/246.33	0.38	0.08	0.08	0.00	1.17	0.00	0.00	0.00	0.00	94.93	3.37	100.00	0.00
R18	811.05/245.77	6.23	0.90	2.69	0.22	29.15	0.08	0.06	0.05	0.01	7.24	38.63	85.25	14.75
R19	808.75/245.08	45.17	7.15	6.44	2.59	0.16	2.33	0.00	0.47	0.02	25.00	0.93	90.28	9.72
R20	807.15/244.60	26.04	4.59	4.75	2.36	0.04	1.17	0.63	0.25	0.02	51.59	0.58	92.02	7.98
R21	804.25/243.71	30.55	2.74	0.54	1.38	0.26	0.39	0.00	0.07	0.01	56.65	1.78	94.36	5.64
R22	798.15/241.86	41.68	5.65	7.64	2.25	11.12	1.65	0.00	0.23	0.02	3.29	16.68	90.21	9.79
R23	797.65/241.71	34.62	3.54	6.20	1.40	19.70	0.97	0.00	0.12	0.02	2.56	24.13	93.26	6.74
R24	794.90/240.88	0.10	0.05	0.00	0.10	27.64	0.00	0.00	0.00	0.01	2.78	40.17	70.86	29.14
R25	792.15/240.05	0.15	0.03	2.07	0.09	31.51	0.00	0.03	0.00	0.01	14.34	43.93	92.15	7.85
R26	789.35/239.20	0.20	0.02	0.06	0.11	32.44	0.00	0.05	0.00	0.01	0.00	47.06	79.94	20.06
R27	786.25/238.26	47.85	6.67	11.17	3.18	8.51	1.15	0.08	0.30	0.02	0.00	7.12	86.05	13.95
R28	782.20/237.03	53.57	7.40	8.72	2.45	4.76	1.48	0.08	0.36	0.01	7.24	5.21	91.29	8.71
R29	781.30/236.76	52.27	9.09	11.65	3.25	1.51	1.76	0.00	0.56	0.02	2.04	2.31	84.46	15.54
R30	778.15/235.80	4.20	0.74	17.53	0.29	27.18	0.19	0.17	0.05	0.02	0.33	1.29	51.98	48.02
R31	776.50/235.30	1.60	0.25	16.80	0.22	28.99	0.05	0.03	0.01	0.02	0.00	2.44	50.39	49.61
R32	755.90/229.06	35.10	4.11	4.34	1.63	24.45	1.56	0.00	0.11	0.06	1.67	1.65	74.68	25.32
R33	754.20/228.55	61.16	9.41	11.66	2.02	1.17	2.16	1.04	0.37	0.01	0.00	1.63	90.63	9.37

Table IV-1. Major Element Compositions (continued)

Sample ID	Depth ft/m	SiO_2	Al_2O_3	MgO	FeO	CaO	K_2O	Na_2O	TiO_2	MnO	NaCl	SO_3	Total	H_2O+CO_2
R34	751.20/227.64	48.66	7.88	9.78	2.82	6.78	2.03	0.00	0.35	0.02	2.12	6.07	86.51	13.49
R35	745.95/226.05	50.64	8.85	10.78	2.66	3.27	2.49	0.15	0.46	0.02	4.45	2.26	86.02	13.98
R36	739.25/224.02	1.26	0.14	0.82	0.12	32.35	0.00	0.04	0.00	0.01	0.00	37.29	72.03	27.97
R37	720.25/218.26	1.24	0.04	2.85	0.11	32.02	0.00	0.03	0.00	0.01	4.94	38.79	80.03	19.97
R38	710.20/215.21	0.89	0.09	1.08	0.11	32.03	0.00	0.08	0.00	0.01	0.00	44.43	78.72	21.28
R39	690.30/209.18	0.16	0.30	0.43	0.10	33.04	0.00	0.03	0.00	0.01	3.98	46.92	84.96	15.04
R40	679.10/205.79	0.30	0.06	1.03	0.10	32.87	0.00	0.05	0.00	0.01	0.00	44.16	78.56	21.44
R41	673.25/204.02	0.22	0.04	0.43	0.10	30.68	0.00	0.03	0.00	0.01	0.00	39.98	71.50	28.50
R42	671.30/203.42	7.34	1.08	13.10	0.31	23.67	0.28	0.03	0.01	0.02	4.75	6.50	57.10	42.90
R43	651.80/197.52	10.30	1.64	14.90	0.53	27.30	0.42	0.22	0.07	0.02	0.00	9.66	65.05	23.96
R44	649.25/196.74	8.11	1.03	10.25	0.33	23.70	0.33	0.05	0.10	0.02	0.00	13.82	57.72	42.28
R45	647.55/196.23	0.36	0.07	0.26	0.12	30.57	0.00	0.03	0.00	0.01	0.00	44.64	76.04	34.95
R46	630.15/190.95	44.21	5.35	3.39	2.10	13.89	2.27	0.12	0.27	0.02	0.36	15.14	87.12	12.88
R47	629.15/190.65	52.16	7.69	5.47	2.27	7.46	2.38	0.00	0.38	0.02	0.56	6.94	85.34	14.66
R48	627.20/190.06	56.49	10.28	7.86	3.53	3.13	3.07	0.10	0.48	0.03	0.62	1.31	86.90	13.10
R49	620.15/187.92	56.29	10.33	9.32	3.14	1.25	2.35	0.00	0.54	0.02	0.69	2.05	85.97	14.03
R50	619.15/187.62	53.14	8.63	8.56	2.22	4.96	2.24	0.07	0.41	0.02	0.67	1.33	82.25	17.75
R51	618.40/187.40	0.81	0.15	0.48	0.12	29.94	0.00	0.04	0.00	0.01	0.00	43.96	75.51	24.49
R52	609.70/184.76	0.77	0.14	0.67	0.11	32.61	0.00	0.03	0.00	0.01	0.20	46.99	81.54	18.46

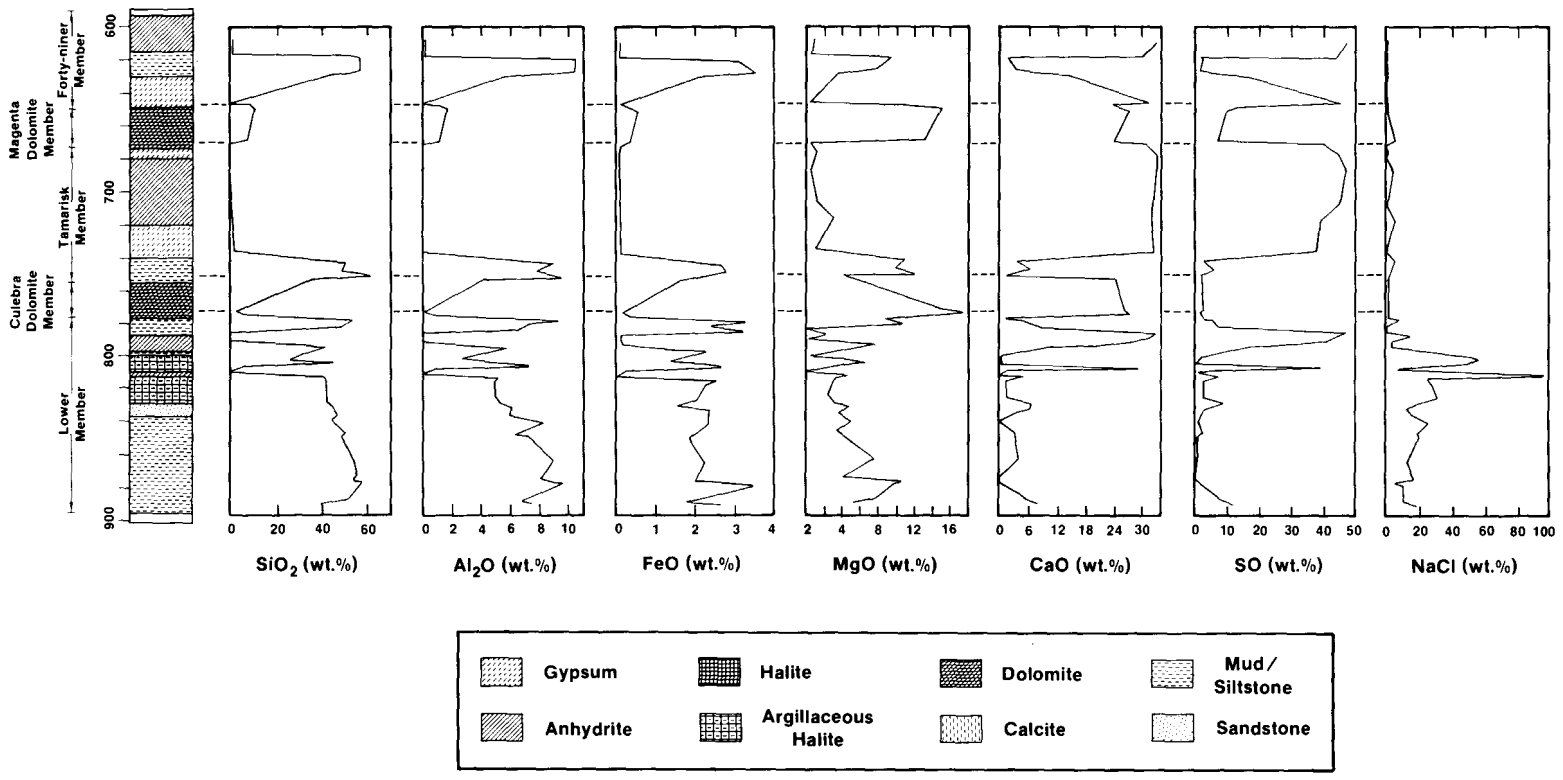

TRI-6342-532-0

Figure IV-1. Major Compositional Components of WIPP-19 Samples.

evaporite precipitation, particularly in the Tamarisk member. The graphs of SiO_2, Al_2O_3, and FeO concentrations have similar trends. The sources of these three components are clastic material brought in by rivers, which drained into the Delaware Basin. There are five major episodes of clastic material influx. Mudstone #1 and mudstone #2, which may have been separated by a substantial halite deposit, since dissolved, comprise the first; this is followed by a period of halite deposition and the second episode (mudstone #3); an evaporite period gypsum/anhydrite deposition; followed by the third clastic episode (mudstone #4). An evaporite interval of dolomite deposition is followed by the fourth interval (mudstone #5), after which a long period of gypsum/anhydrite deposition occurred. The final clastic episode (mudstone #6) is followed by additional gypsum/anhydrite deposition.

The graph of the concentration of magnesium versus depth of sample is not as readily understood as those of the purely clastic minerals, such as SiO_2. Magnesium is an important constituent of seawater and a relatively minor one in terrigenous sources of clastic material. The graph, however, indicates that the sediments deposited during those periods of time that were dominated by clastic (freshwater source) input have high magnesium concentrations (up to 18 wt.%). The high magnesium concentrations can be explained by two factors: diagenetic alteration of clay minerals, and the formation of magnesite, both as a primary precipitate and as a replacement mineral. The first of these factors is by far the more important one: once a normal assemblage of clay minerals (typically illite, dioctahedral smectite, kaolinite and chlorite) is deposited in a basin that contains hypersaline brines rich in magnesium, the clay minerals begin to alter (halmyrolysis). Upon compaction and burial with pore fluids also rich in magnesium, the alteration continues, and in some cases the detrital clay minerals form new species, all of which contain more magnesium than their precursors. The uptake of magnesium is concomitant with a loss of aluminum and silicon; these elements form authigenic phases.

The magnesium concentration in the two dolomite members (Culebra and Magenta) is, of course, also high, although the Culebra was not well sampled in this study. The dolomite deposits may have been primary (see, for example, Parry et al., 1970) or the result of early dolomitization of precursor calcite.

Calcium in these sediments is derived almost entirely from dissolved Ca^{2+} in sea and fresh water. It is deposited mainly as the minerals gypsum (which may, in turn, dehydrate to anhydrite) and either calcite or dolomite. The CaO profile in Figure IV-1 shows that the concentration has an almost perfect negative correlation with the purely clastic components (SiO_2, Al_2O_3, FeO).

The sulfur concentration profile, when compared to the calcium concentration, makes the distinction between episodes of calcite/dolomite deposition and gypsum/anhydrite deposition. Finally, the NaCl plot shows a trend of overall decreasing total salinity from the bottom of the formation to the top.

V. WHOLE ROCK MINERALOGICAL DATA

The individual mineral constituents were identified by x-ray diffraction (XRD) analysis, and their modes (weight percent) were determined initially by semi-quantitative XRD analysis and then by back calculation (sequential inversion) from the compositional data presented in the previous chapter.

X-Ray Diffraction Analysis

The details of the procedures used in the XRD identification procedure are discussed in Appendix A. All 52 samples were so analyzed. In most cases, whole rock powders were used; however, in some cases the H_2O insoluble residue was analyzed. Minerals identified include halite, gypsum, anhydrite, dolomite, calcite, aragonite, magnesite, quartz, feldspar, and clay. The results of the XRD identification and semi-quantitative analysis procedures are summarized in Table V-1.

Calculated Mineral Modes

The method used to calculate the mineral modes, which uses both the results of the XRD identification process and the complete set of compositional data presented in the previous chapter, is discussed in detail in Appendix B. The results of these calculations are shown in Table V-2.

Plots of the mineral modes versus sample depth in the column are shown in Figure V-1; a stratigraphic column is included for comparison. These plots of mineral abundances show very similar trends to those of the major elements (Figure IV-1). Once again the 5 major clastic input events are separated by periods of evaporite deposition; this can be readily seen in the plots for quartz and clay versus sample depth. Dolomite deposition occurs in 2 major events, the 2 dolomite members of the formation, Culebra and Magenta. Dolomite also occurs in small amounts, up to 15%, usually in rocks dominated by clastic material. Magnesite is restricted to the bottom half of the column and is associated primarily with halite. It is never abundant; the maximum mode is less than 14 weight percent.

The sulfur minerals, gypsum and anhydrite, dominate the upper part of the section; anhydrite is occasionally abundant in the lower part of the core, but is generally restricted to fairly thin beds. The Tamarisk member is a massive gypsum/anhydrite unit with a clastic unit at the bottom. Gypsum and anhydrite replace each other in several places, and it is clear that both transitions,

Table V-1. Summary of XRD Identification and Semi-Quantitative Analysis of WIPP-19 Samples: XXX = Very Abundant. XX = Abundant. X = Present. tr = Trace

ID	Clay	Quartz	K-spar	Calcite	Argonite	Dolomite	Gypsum	Anhydrite	Magnesite	Halite
R1	XX	X	tr					XX		X
R2	XX	XX	tr					X	X	X
R3	XX	XX	tr						X	X
R4	XX	XX	tr						X	X
R5	XX	XX	tr						X	tr
R6	XX	XX	tr			X				X
R7	XX	XX	tr			X		tr		X
R8	XX	XX	X			X		tr		X
R9	XX	XX	tr							XX
R10	XX	XX	tr			X		X		X
R11	XX	XX	tr			X		X		X
R12	XX	XX	tr					X	X	X
R13	XX	XX	tr			tr		X		XX
R14	XX	XX						X		XX
R15								X		XX
R16										XXX
R17		tr						X		XXX
R18	tr	X						XXX		tr
R19	XX	XX	tr					X		XX
R20	XX	X	tr							XX
R21	XX	X						tr		XXX
R22	XX	XX	tr					X	X	X
R23	XX	XX						XX	tr	X
R24								XXX		tr
R25								XXX	X	tr
R26							tr	XXX		
R27	XXX	X					X	tr		
R28	XXX	XX					tr			tr
R29	XXX	XX					tr			tr
R30	tr	X				XXX				
R31	tr	X				XXX				X
R32	XXX	X		XX						tr
R33	XXX	XX	X				tr	tr		
R34	XXX	XX	tr				X	tr		tr
R35	XX	XX	tr		tr		tr			tr
R36							XXX			
R37							X	XXX		tr
R38								XXX		
R39								XXX		tr
R40							tr	XXX		
R41							XXX			
R42	tr	X				XXX	tr			tr
R43	tr	X				XXX	X			
R44	X	X	tr			XXX	X			
R45							XXX			
R46	XX	XX	tr				X			
R47	XX	XX	tr				tr			
R48	XX	XX				X				
R49	XXX	XX	X				tr			
R50	XX	XX	tr			X	tr			
R51		tr					XXX			
R52								XXX		

Table V-2. Calculated Mineralogical Modes

ID	Quartz	Clay	Dolomite	Gypsum	Anhydrite	Magnesite	Halite	Total
R1	23.60	40.88	0.00	0.00	19.77	0.00	16.94	101.20
R2	35.46	38.61	0.00	0.00	13.38	6.16	10.39	104.01
R3	36.59	52.63	0.00	0.00	0.00	11.70	10.41	111.33
R4	34.62	48.67	0.00	0.00	0.00	13.64	5.08	102.00
R5	37.63	44.82	0.00	0.00	0.00	0.00	16.41	98.86
R6	34.43	49.17	11.11	0.00	1.26	0.00	12.70	108.66
R7	33.27	39.06	7.00	0.00	1.98	0.00	19.72	101.02
R8	36.65	35.03	5.13	0.00	4.24	0.00	19.03	100.08
R9	27.12	45.32	0.00	0.00	1.90	0.00	25.76	100.09
R10	34.64	32.59	4.92	0.00	3.96	0.00	16.16	92.26
R11	32.57	33.26	14.56	0.00	5.22	0.00	12.54	98.14
R12	31.51	28.59	0.00	0.00	14.17	0.83	18.37	93.48
R13	32.45	27.07	0.00	0.00	3.92	0.00	30.85	94.29
R14	31.86	27.17	0.00	0.00	4.75	0.00	27.40	91.18
R15	29.75	28.15	0.00	0.00	11.54	0.00	24.78	94.22
R16	0.06	0.39	0.00	0.00	1.60	0.00	98.49	100.53
R17	0.21	0.44	0.00	0.00	5.72	0.00	94.93	101.30
R18	4.29	4.99	0.00	0.00	65.67	0.00	7.24	82.19
R19	29.68	39.73	0.00	0.00	1.59	0.00	25.00	96.00
R20	16.10	25.48	0.00	0.00	0.99	0.00	51.59	94.17
R21	24.62	15.20	0.00	0.00	3.03	0.00	56.65	99.49
R22	29.44	31.39	0.00	0.00	28.36	7.08	3.29	99.55
R23	26.95	19.67	0.00	0.00	41.02	7.39	2.56	97.59
R24	0.00	0.28	0.00	0.00	68.30	0.00	2.78	71.36
R25	0.08	0.18	0.00	0.00	74.68	4.29	14.34	93.56
R26	0.15	0.13	0.00	3.16	77.56	0.00	0.00	81.00
R27	33.40	37.05	0.00	15.32	1.50	0.00	0.00	87.27
R28	37.53	41.12	0.00	11.21	0.00	0.00	7.24	97.11
R29	32.58	50.50	0.00	4.96	0.00	0.00	2.04	90.07
R30	2.61	4.09	87.54	2.76	0.00	0.00	0.33	97.34
R31	1.01	1.38	90.35	5.24	0.00	0.00	0.00	97.97
R32	26.19	22.84	41.58	3.54	0.00	0.00	1.67	95.82
R33	40.77	52.28	0.00	3.51	0.00	0.00	0.00	96.55
R34	31.60	43.75	0.00	11.82	1.56	0.00	2.12	90.85
R35	31.47	49.16	0.00	4.86	0.00	0.00	4.45	89.93
R36	0.96	0.78	0.00	80.20	0.00	0.00	0.00	81.93
R37	1.15	0.22	0.00	27.78	55.56	0.00	4.94	89.65
R38	0.70	0.51	0.00	0.00	75.54	0.00	0.00	76.74
R39	0.09	0.18	0.00	0.00	79.77	0.00	3.98	84.02
R40	0.17	0.33	0.00	3.75	71.31	0.00	0.00	75.56
R41	0.13	0.25	0.00	85.98	0.00	0.00	0.00	86.35
R42	4.99	6.03	63.53	13.98	0.00	0.00	4.75	93.27
R43	6.75	9.11	68.15	20.77	0.00	0.00	0.00	104.78
R44	5.88	5.70	46.30	29.71	0.00	0.00	0.00	87.60
R45	0.21	0.39	0.00	96.00	0.00	0.00	0.00	96.59
R46	32.62	29.73	0.00	32.56	0.00	0.00	0.36	95.27
R47	35.50	42.74	0.00	14.93	0.00	0.00	0.56	93.72
R48	34.22	57.09	7.33	2.83	0.00	0.00	0.62	102.09
R49	33.92	57.36	0.00	4.41	0.00	0.00	0.69	96.38
R50	34.44	47.95	13.39	2.86	0.00	0.00	0.67	99.32
R51	0.48	0.84	0.00	94.54	0.00	0.00	0.00	95.86
R52	0.46	0.80	0.00	0.00	79.88	0.00	0.20	81.34

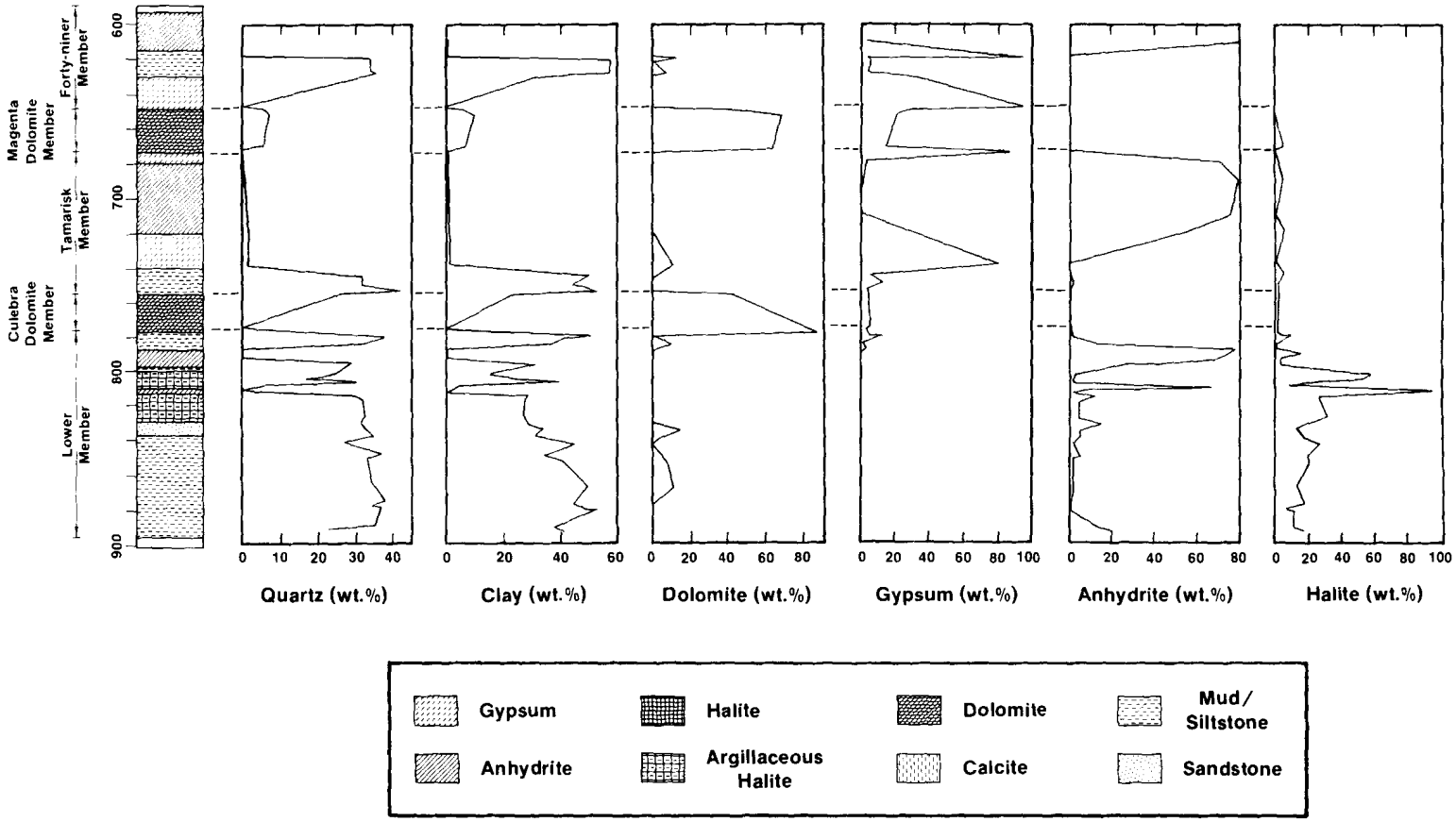

TRI-6342-476-0

Figure V-1. Mineralogical Modes of WIPP-19 Samples.

from gypsum to anhydrite and from anhydrite to gypsum, have occurred (see Chapter VI).

Halite is fairly abundant only throughout the grey siltstone (mudstone #2) at the bottom of the section, becoming the dominant mineral at the top of this unit, where argillaceous halite and a thin bed of relatively pure halite occur. Halite abundance diminishes considerably above this point and becomes a relatively insignificant component in the upper part of the formation.

VI. PETROGRAPHY

Individual core samples were examined and described, and petrographic thin sections of all core samples were studied under the optical microscope. Polished thin sections from selected samples were prepared for use under the electron microprobe. This chapter will describe the habits and morphology of the individual minerals.

Evaporite Minerals

HALITE

Halite in the Rustler Formation occurs in four basic textural environments. The first mode of occurrence, bedded halite (Figure VI-1), is characterized by large, equant, subhedral grains, which are typical of recrystallized halite (Hovorka, 1983). Typical grain size is 2 to 20 mm (.08 to .80 in.) in lateral dimensions; the color is pale orange, probably due to the presence of very small quantities of polyhalite and/or hematite. In thin section, bedded halite displays irregular grain boundaries and numerous impurities, the most common being magnesite (nodules and platy euhedral crystals) and anhydrite grains. Occasional bivalve filaments (Figure VI-2), now composed of magnesite, occur.

"Displacive" halite (Figure VI-3) forms by rapid growth of large (1 to 20 mm) (.003 to .80 in.) halite crystals within a predeposited terrigenous clastic sediment bed (Hovorka, 1983). The halite crystals are normally euhedral and display cubic structures in thin section (Figure VI-4). The most common impurity in the displacive halite is magnesite, both as nodules and euhedral laths.

Halite as a cement in mud/siltstones is common in the lower member of the Rustler Formation. It occurs as a void-filling matrix that often preserves the original lamination of the mud/siltstone, indicating that the precipitation of halite in the pore space occurred after deposition of the clastic material. However, in some samples, the original structure of the siliclastic material has been destroyed, leaving a chaotic interclastic texture (Hovorka, 1983), indicating that some dissolution of halite may have occurred or that the disruption may be due to the displacive growth of halite itself ("haloturbation" of Smith, 1971). Hovorka (1983) has concluded that this type of partial dissolution and/or haloturbation is synsedimentary, and thus, halite cement, whether it preserves the original texture of the siliclastic sediment or not, may be considered to be primary.

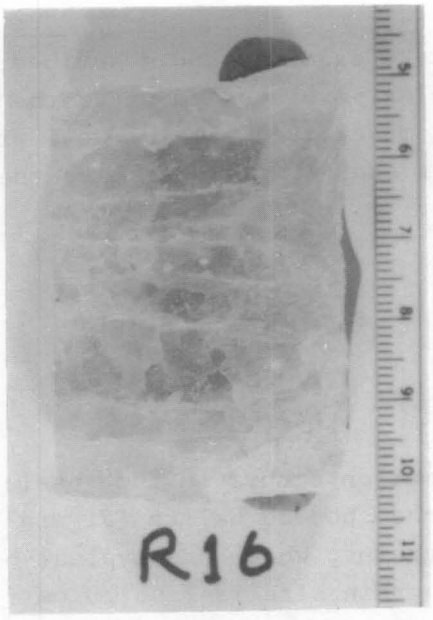

Figure VI-1. Hand Specimen of Bedded Halite, Sample R16. Lower Member, 814 ft (247 m).

Figure VI-2. Bivalve in Halite, Transmitted Light, Crossed Polars. Sample R13, Lower Member, 829 ft (251 m). FOV = 2.9x2.32mm.

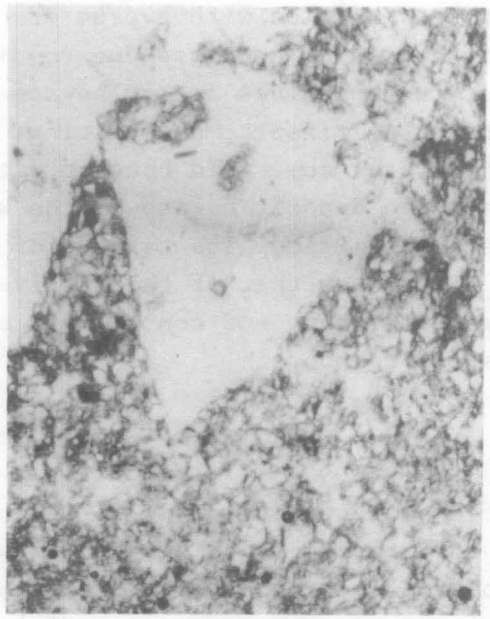

Figure VI-3. Displacive Halite, Transmitted Plane Polarized Light. Sample R13, Lower Member, 829 ft (251 m). FOV=2.9x2.32mm.

Figure VI-4. Cubic Structures in Halite Outlined by Organic Matter. Transmitted plane polarized light. Sample R13, Lower Member, 829 ft (251 m). FOV=2.9x2.32mm.

Fracture-filling halite occurs mainly in the lower member in the WIPP-19 core. Elsewhere, most fractures are filled with gypsum or dolomite. The fractures themselves were probably caused by collapse due to dissolution of halite beds below the fractured members themselves and/or by some minor tectonic events (subsidence, Pennsylvanian to Triassic, and tilting, early Cenozoic; Borns et al., 1983). Later, fresh water coming in contact with halite would become halite saturated and begin to deposit halite on the walls of the fractures until the fracture itself is filled. The texture of the vein and fracture-filling halite is very similar to that of the massive, recrystallized, bedded halite: grains are large and equant and contain few or no fluid inclusions. Mud and silt inclusions are common.

ANHYDRITE

The most common form of occurrence of anhydrite in the WIPP-19 core is a crudely banded nodular structure (Figure VI-5). The upper part of the Tamarisk member is composed almost entirely of this massive nodular anhydrite. The top part of the Forty-niner member and a section of the lower member are also nodular anhydrite (sometimes called "laminated" due to the crude banding, but this should not be confused with deep water laminated anhydrite). The anhydrite in these units is finely crystalline, and the overall color is olive-grey. In thin section (Figure VI-6), nodular anhydrite has a very high relief and birefringence, and individual grains are lath shaped and often grouped in radiating clusters.

In anhydrite sediments that have been gypsified (or regypsified), there are often relict anhydrite crystals, which have resisted hydration. In some cases, the transition from anhydrite to gypsum is clearly recorded in the thin sections (Figure VI-7).

GYPSUM

In the previous section, the transition from anhydrite to gypsum, as seen in thin section, was documented. Although most, if not all, of the calcium sulfate in the Rustler section was probably initially deposited as gypsum (Sonnenfeld, 1984), anhydrite nodules have been found buried only a few feet in recent coastal sabkha environments. The conversion from gypsum to anhydrite upon burial occurs within a temperature range of about 20° to 40°C, depending on the ionic strength of the solution in contact with the solid. Thus, upon burial, gypsum will convert to anhydrite, and great burial depths are not needed. It is probable that most of the gypsum found in the Rustler section is the result of secondary gypsification of anhydrite by meteoric waters (Sonnenfeld, 1984) undersaturated with respect to sulfates.

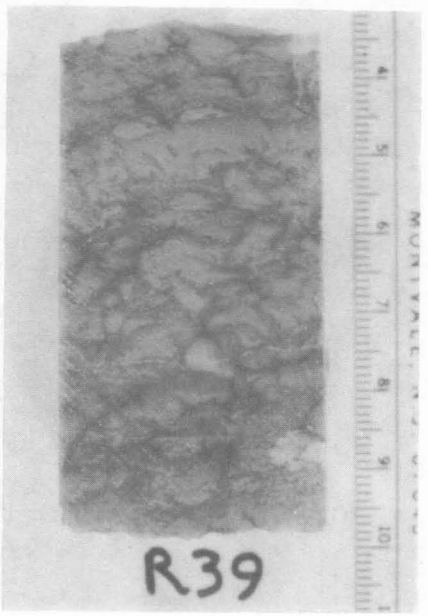

Figure VI-5. Hand Specimen of Massive Nodular Anhydrite. Sample R39, Tamarisk Member, 690 ft (209 m).

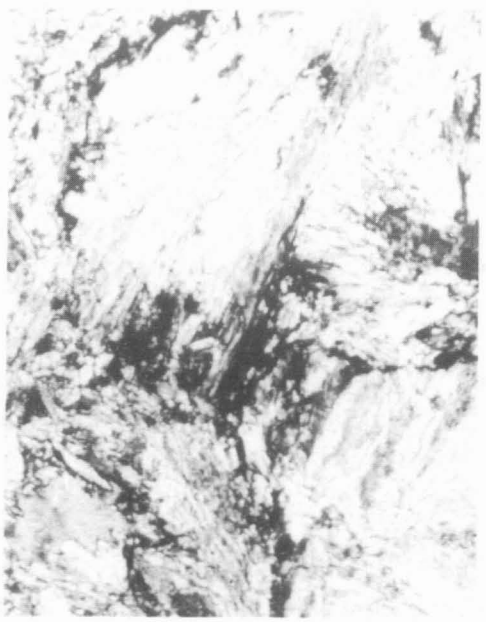

Figure VI-6. Radiating Laths of Anhydrite, Transmitted Plane Polarized Light. Sample R39, Tamarisk Member, 690 ft (209 m). FOV=0.53x0.42mm.

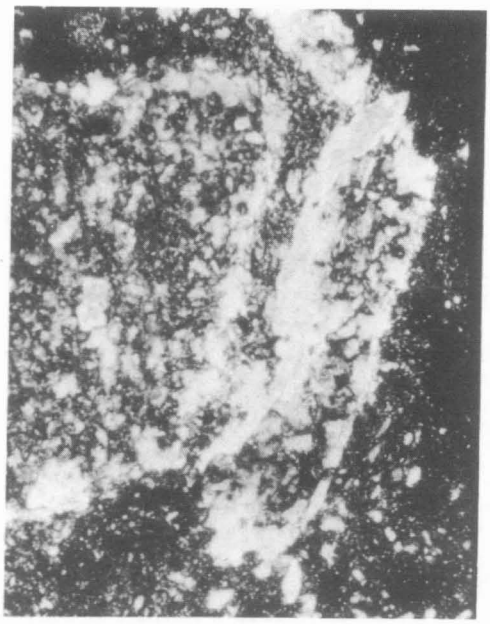

Figure VI-7. Large Anhydrite Lath Altering to Gypsum. Transmitted light, crossed polars. Sample R34, Tamarisk Member, 751 ft (228 m). FOV=2.9x2.32mm.

In hand specimen, gypsum in the WIPP-19 core samples occurs mainly as massive, medium to dark grey, crudely banded forms (Figure VI-8). The banding is defined by gypsum veins and is essentially horizontal. In thin section, 2 basic textures appear: the massive areas are formed by a network of irregular crystals ("patchy" gypsum), whereas the veins are parallel or subparallel to bedding, with fibers aligned at right angles to bedding (Figure VI-9). Crystals are much larger in the fibrous gypsum than in the patchy areas. Presumably, the veins formed conduits for the fluids, which caused the hydration of the anhydrite in the first place; these veins were later cemented with $CaSO_4$ dissolved during hydration of anhydrite without incurring a very large volume increase, which would have disrupted the original bedding in a catastrophic way.

Veins filled with fibrous gypsum commonly occur in dolomite, mud/siltstone, and even halite, so the excess $CaSO_4$ resulting from the hydration process is probably distributed throughout the section.

Ripple-laminated gypsum (Figure VI-10) occurs in one sample. Beds of finely-laminated light brown gypsum alternate with darker gypsum; open fractures occur between laminae (these may have been caused by the core drilling process). Individual ripple sets are 0.2 to 0.8 cm (0.08 to 0.31 in.) thick. A similar sample, found in the Upper Permian Alibates Formation in the Texas Panhandle, is described by McGillis and Presley (1981).

DOLOMITE

Dolomite occurs mainly in the two dolomite members, Culebra and Magenta, as unfossiliferous, laminated, fine-grained dolomicrite. It is generally buff to light brown in color (Figure VI-11). The laminae consist of areas of lighter and darker colored dolomite, the color being dependent on the amount of clay and organic matter in the dolomite matrix. Voids in the form of vugs (0.02 to 1 cm in diameter) (0.008 to 0.39 in.) are common; many of the vugs adjacent to fractures are filled with gypsum and occasionally with halite. Open vugs are usually lined with powdery clay and dolomite. Veins and fractures are common; they are usually filled with fibrous gypsum, whereas open fractures, along which fluids have apparently been recently moving, are lined with clay. In thin sections, dolomite is microcrystalline (Figure VI-12) and shows the very high relief and high birefringence typical of carbonates. Individual crystals range in lateral dimension from about 2 to 20 microns. Dark areas of clay and organic matter usually occur as wisps or blotches, but occasionally as laminae.

MAGNESITE

Magnesite is a fairly minor component, never exceeding 15% of the samples examined in this study. It occurs in two textural styles: as microcrystalline

Figure VI-8. Hand Specimen of Massive Gypsum. Sample R45, Forty-niner Member, 647 ft (196 m).

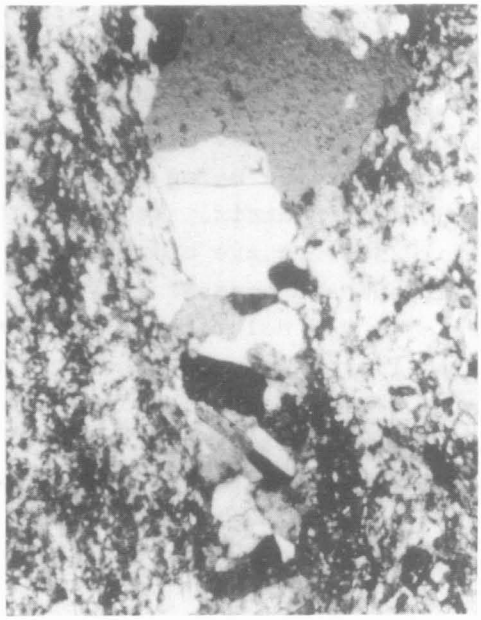

Figure VI-9. Fibrous Gypsum Vein in "Patchy" Gypsum. Transmitted light, crossed polars. Sample R36, Tamarisk Member, 739 ft (224 m). FOV = 2.9x2.32mm.

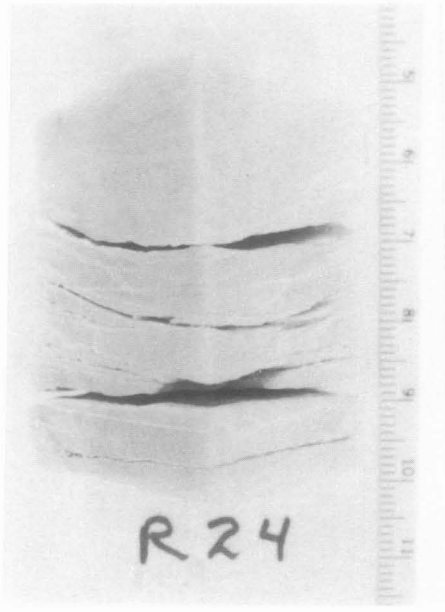

Figure VI-10. Hand Specimen of Ripple Laminated Gypsum. Sample R24, Lower Member, 795 ft (241 m).

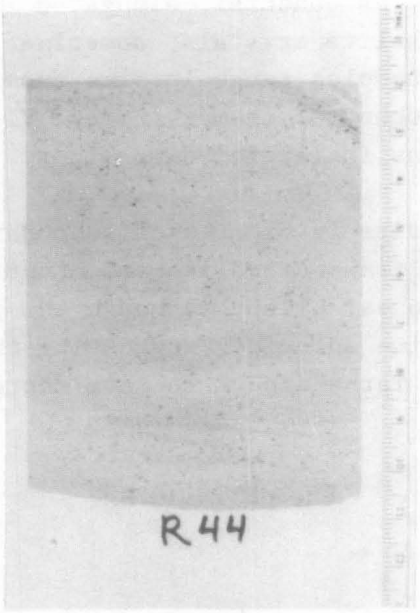

Figure VI-11. Hand Specimen of Massive Dolomite. Sample R44, Forty-niner Member, 749 ft (227 m).

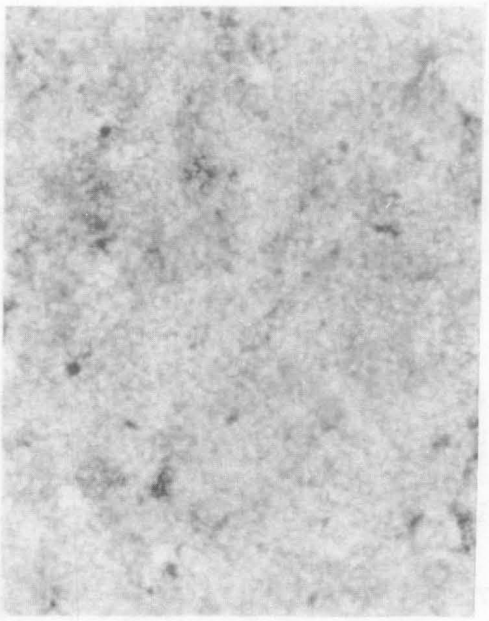

Figure VI-12. Dolomicrite. Transmitted light, crossed polars. Sample R41, Forty-niner Member, 673 ft (204 m). FOV = 0.2x0.16mm.

nodules, which are usually contained in either a halite or mud/siltstone matrix (Figure VI-13), and as euhedral, elongated laths (Figure VI-14), which always occur embedded in halite crystals, sometimes in conjunction with anhydrite crystals. The nodules range in size from 20 to 100 microns; the individual crystals are subhedral rhombs (Figure VI-15), which are generally not greater than 10 microns in lateral dimensions.

The nodular form of magnesite is clearly of secondary origin (Figure VI-13), since the nodule outlines transect halite and anhydrite crystal boundaries. The origin is difficult to establish, although the grain size is similar to that of the microcrystalline dolomite, suggesting that magnesite may have had a calcite precursor. The laths appear to have coprecipitated with the halite.

Clastic Minerals

QUARTZ

Quartz is a major mineral constituent of the Rustler Formation. With the exception of the Tamarisk anhydrite member and the Culebra and Magenta Dolomites, it ranges in abundance from about 5% to 60%. More than 99% of the quartz seen in thin section is of detrital origin; the detrital grains range in lateral dimensions from less than 1 micron up to about 100 microns. They are generally angular in shape and always occur in association with clay.

Authigenic quartz is a fairly common, though minor component of some samples. It occurs in association with halite, usually at the boundaries between halite and clay/quartz-rich areas. The grains are relatively large (Figure VI-16); lateral dimensions range from about 20 to 200 microns, and normally have uncorroded facets. Much larger grains of authigenic quartz have been found in samples from the Salado Formation (Stein, 1985).

FELDSPAR

X-ray diffraction analysis shows the presence of feldspar in small quantities in most of the samples that contain clay and quartz. Microprobe analyses (Chapter VII) show that the feldspar is predominantly potassic, although a few grains of nearly pure albite were identified.

Feldspar grains are very similar in shape and size to the quartz grains that invariably surround them. Like quartz, they are predominantly of detrital origin. However, authigenic feldspar also occurs in conjunction with argillaceous halite (Figure VI-17). The grains are also quite large (up to 200 microns in lateral dimensions), and the facets frequently are corroded and irregular.

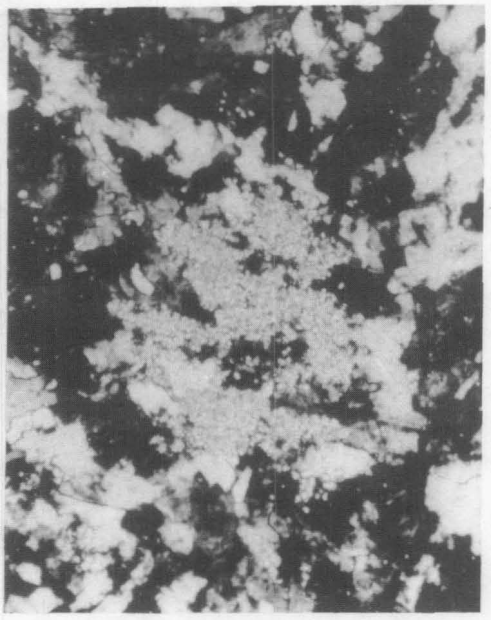

Figure VI-13. Magnesite Nodule. Transmitted light, crossed polars. Sample R25, Lower Member, 792 ft (240 m). FOV=2.9x2.32mm.

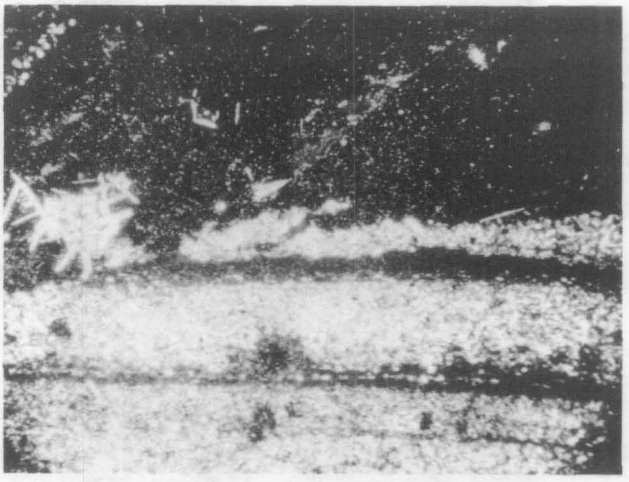

Figure VI-14. Magnesite Laths in Halite. Transmitted light, crossed polars. Sample R13, Lower Member, 829 ft (251 m). FOV=2.9x2.32mm.

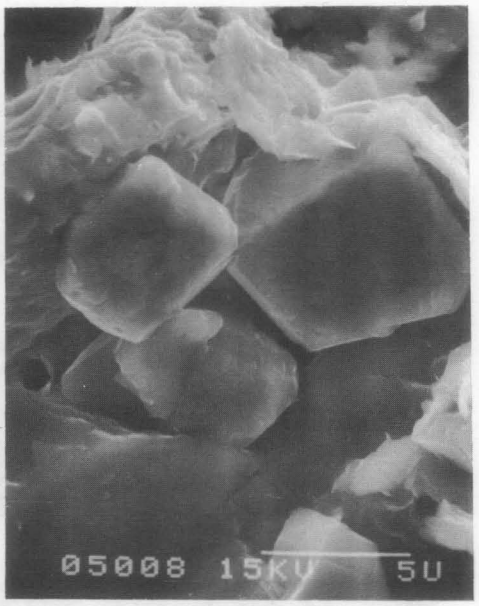

Figure VI-15. SEM Photomicrograph in Secondary Electrons of Magnesite Grains in Nodule. Sample R5, Lower Member, 878 ft (266 m).

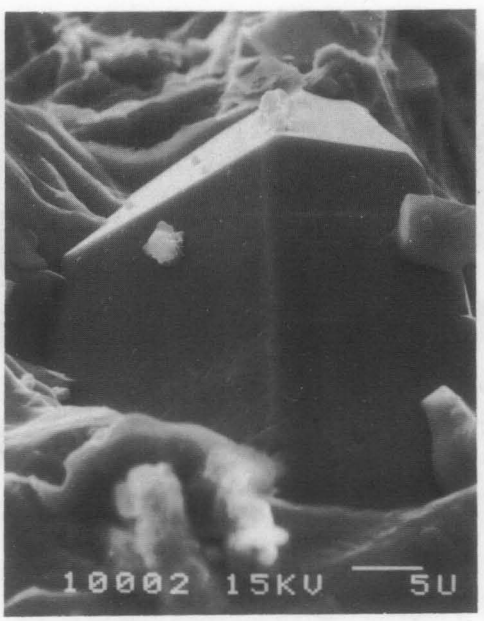

Figure VI-16. SEM Photomicrograph in Secondary Electrons of Authigenic Quartz Grain. Sample R15, Lower Member, 817 ft (248 m).

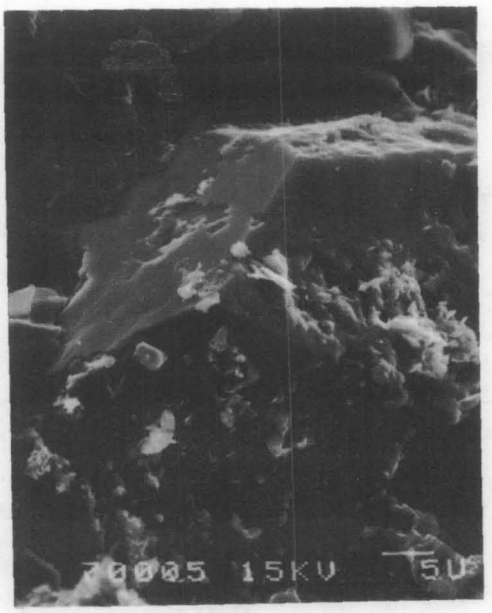

Figure VI-17. SEM Photomicrograph in Secondary Electrons of Authigenic Potassium Feldspar Grain. Sample R7, Lower Member, 852 ft (258 m).

DETRITAL PHYLLOSILICATE GRAINS

Phyllosilicate grains of metamorphic origin constitute a minor component of mud/siltstones in the Rustler Formation. Four phases have been identified: muscovite, high and low iron chlorite, and biotite. Figures VI-18 to VI-20 show typical examples of these grains.

CLAY

Like quartz, clay is a major component of the Rustler Formation, and is roughly equal in abundance to quartz. Clay almost always occurs in direct association with quartz, feldspar, and detrital phyllosilicate grains, showing a common origin for these particles.

In mud/siltstones, in which the primary bedding lamination has been preserved, such as sample R10 (Figures VI-21 and VI-22), the lamination is demarcated by alternating layers of clay-rich/quartz-poor and clay-poor/quartz-rich material. Both layers are cemented with halite.

Disrupted lamination, shown in sample R11 (Figure VI-23), is indicative of collapse deformation due to dissolution of halite beds and is a fairly common feature. When clay and silt bearing halite is dissolved, the result is a layer of mud/silt draped around other insoluble materials (Hovorka, 1983). A chaotic mud/siltstone texture (Figure VI-24) devoid of any lamination is

probably caused by dissolution of mud and silt-bearing halite (argillaceous halite).

Trace and Accessory Minerals

CALCITE

Calcite occurs in only one sample, R32, located just above the Culebra Dolomite. Calcite constitutes about 45% of the bulk sample; it is microcrystalline in texture (Figure VI-25), and the grain size is very similar to that of the dolomite samples. It is intermixed with clay and quartz, which preserve bedding laminations and appear to have been disrupted by dissolution. Both the clay/quartz and calcite are cemented with halite.

Since the calcite lies on top of the Culebra Dolomite, which is extremely fractured and has water moving through the fractures, it is reasonable to suppose that the calcite in this sample is the product of alteration ("dedolomitization") of dolomite, rather than being a primary deposit.

Figure VI-18. SEM Photomicrograph in Secondary Electrons of Muscovite Grain in Thin Section. Sample R8, Lower Member, 851 ft (258 m).

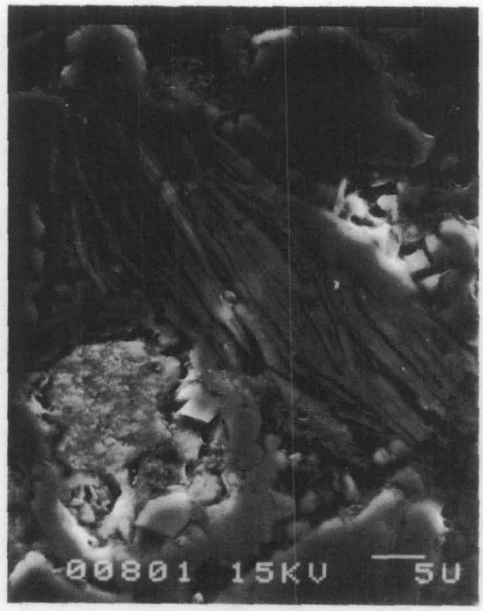

Figure VI-19. SEM Photomicrograph in Secondary Electrons of High-Iron Chlorite Grain in Thin Section. Sample R8, Lower Member, 851 ft (258 m).

Figure VI-20. SEM Photomicrograph in Secondary Electrons of Low-Iron Chlorite Grain in Thin Section. Sample R7, Lower Member, 852 ft (258 m).

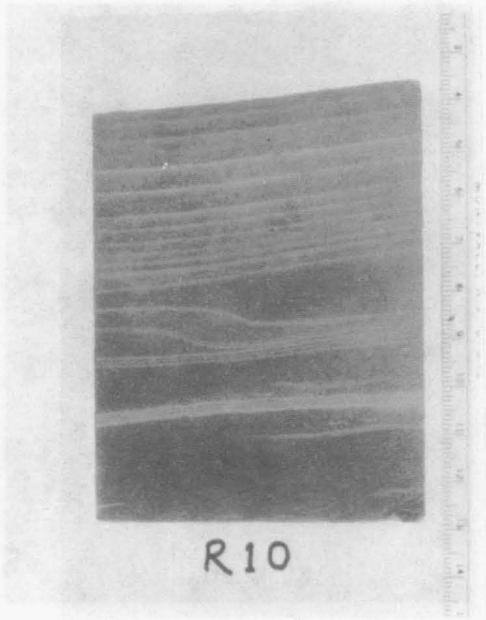

Figure VI-21. Hand Specimen of Laminated Mudstone. R10, Lower Member, 839 ft (254 m).

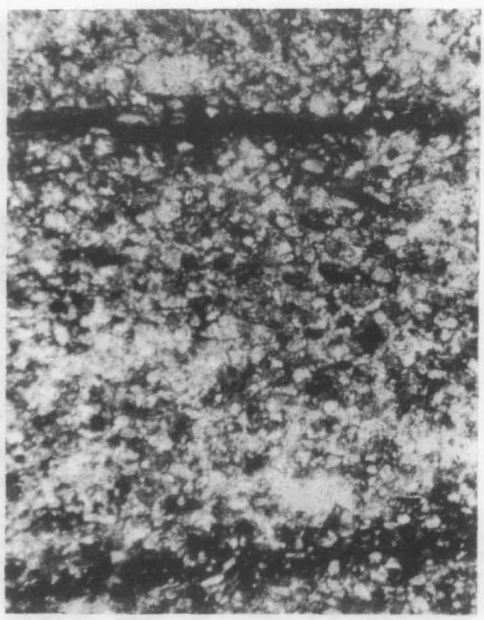

Figure VI-22. Mud/Siltstone Showing Laminae. Transmitted light, crossed polars. Sample R10, Lower Member, 839 ft (254 m). FOV = 2.9x2.32mm.

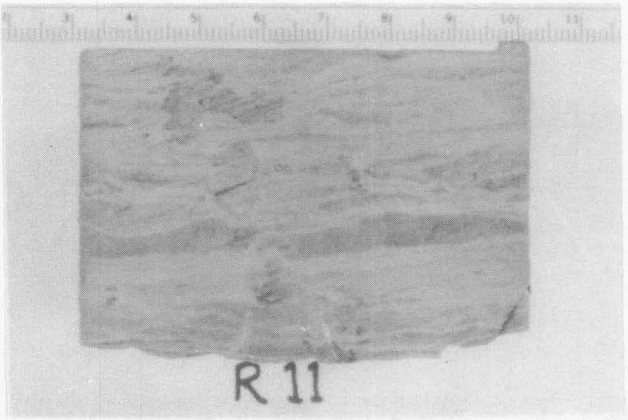

Figure VI-23. Hand Specimen Showing Disrupted Lamination. Sample R11, Lower Member, 835 ft (253 m).

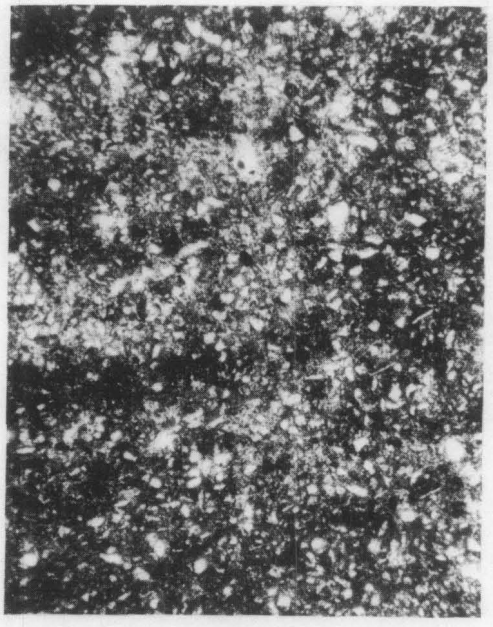

Figure VI-24. Chaotic Mud/Siltstone. Transmitted light, crossed polars. Sample R48, Forty-niner Member, 627 ft (190 m). FOV=2.9x2.32mm.

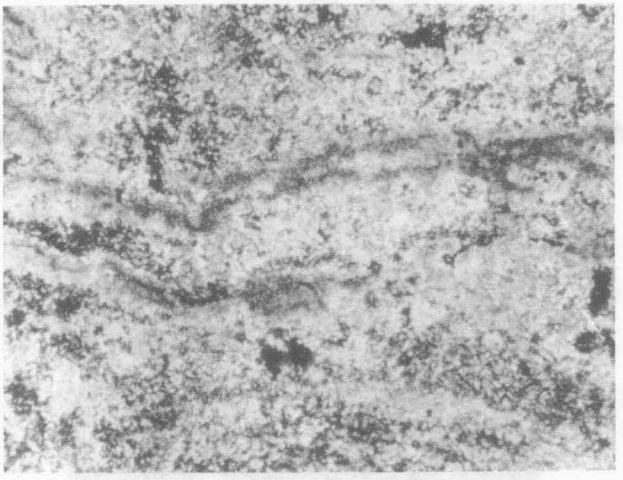

Figure VI-25. Calcite with Clay Veins. Transmitted light, crossed polars. Sample R32, Tamarisk Member, 756 ft (229 m). FOV=2.9x2.32mm.

PYRITE

Pyrite is a common accessory mineral in many of the samples from the WIPP-19 core. Scanning electron microscope (SEM) micrographs (Figure VI-26) show that the grains are euhedral to subhedral rhombs with facets that are often pitted. Grain sizes range from 2 to 15 microns lateral dimensions.

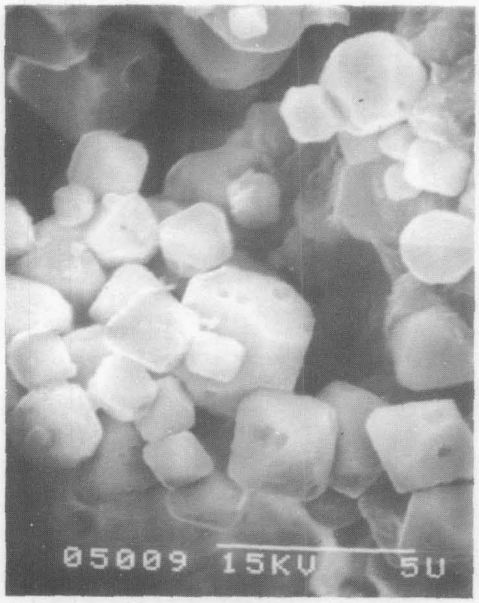

Figure VI-26. SEM Photomicrograph in Secondary Electrons of Pyrite Grains. Sample R3, Lower Member, 881 ft (267 m).

VII. MINERAL COMPOSITIONS

Electron microprobe analysis (EMX) was used to determine the compositions of most of the minerals present in the polished thin sections prepared for this study. Analytical methods are described in Appendix A. The results of these analyses are presented below.

Evaporite Minerals

HALITE

Due to rapid decrepitation and/or volatilization of halite under the electron beam, it was not possible to obtain wavelength dispersive spectrometer (WDS) analyses of halite. Energy dispersive spectrometer (EDS) spectra were obtained using very brief (5 second) counting times, and these spectra did not reveal the presence of any other component other than sodium and chlorine; it is probably safe to assume that the halite in these samples is nearly pure NaCl.

ANHYDRITE

WDS analyses of anhydrite in several samples from the Rustler section showed that anhydrite grains are nearly pure $CaSO_4$; the abundance of all other elements was below the detection limits of the microprobe.

GYPSUM

As with anhydrite, gypsum in both "patchy" and fibrous forms, is nearly pure $CaSO_4.2H_2O$.

DOLOMITE

No dolomite compositions were obtained from the samples selected for this project; however, in a study of samples from various drill cores of the Culebra Dolomite, Sewards et al. (1991) found that the average calcium to magnesium ratio of 5 samples analyzed was 1.05, and that there were an average of 0.004 atoms of Fe per unit cell. Figure VII-1, taken from that report, shows the Ca to Mg ratio, determined by EMX for the five samples in that study, compared to other evaporite and non-evaporite dolomites.

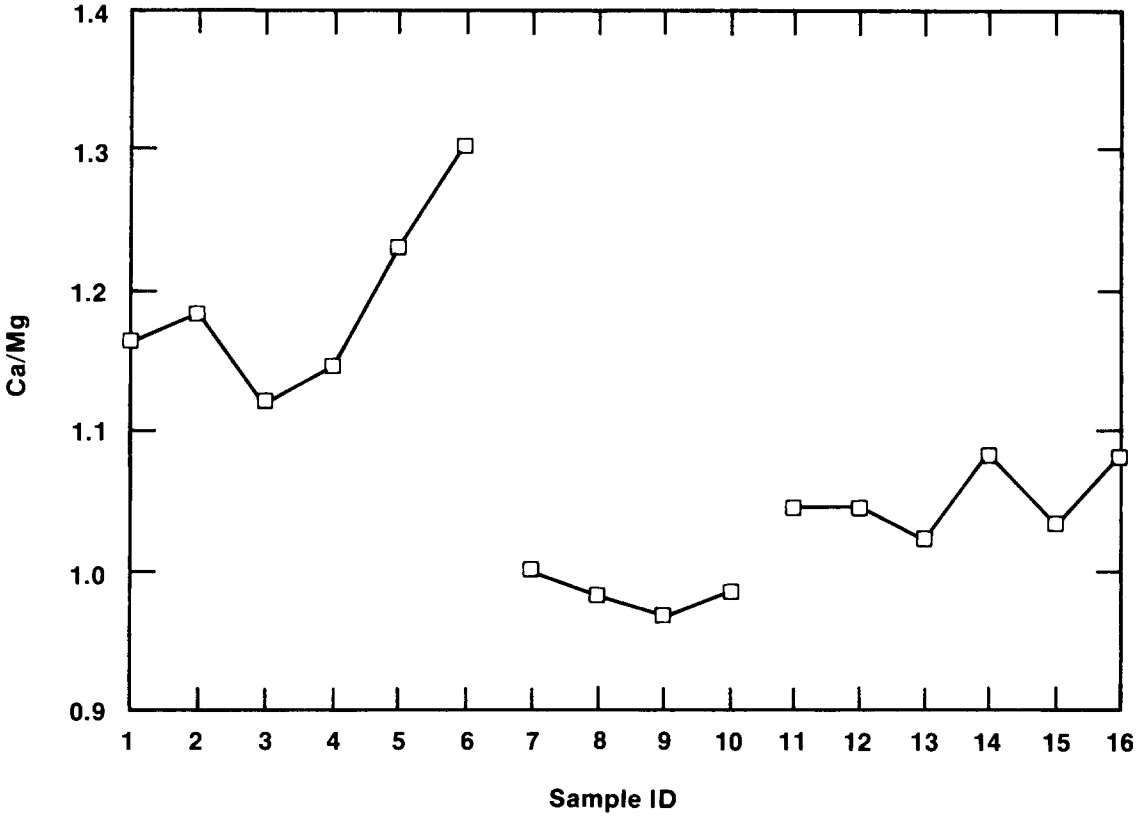

1	G-1322	Galena Platteville Formations, Ordovician, Oglesby, Illinois
2	G-1331	Edgewood Dolomite, Silurian, Pike County, Illinois
3	G-1181	Cogollo Formation, Cretaceous, Venezuela
4	G-379	Inglis Member, Moodys Branch Formation, Upper Eocene, Levy County, Florida
5	G-1055	Avon Park Formation, Middle Eocene, Levy County, Florida
6	G-1138	Funafuti (Pacific Island Core) Depth 840 Feet
7	G-1387	Anhydrite-Dolomite Rock, Permian, Yorkshire
8	G-1187	Salina Formation, Silurian, Michigan
9	G-1121	Evaporite Sequence, Saskatchewan
10	G-1374	Edwards Formation, Early Cretaceous, New Mexico
11	WIPP-12	#1
12	WIPP-12	#2
13	WIPP-12	#9
14	WIPP-12	#12
15	WIPP-12	#16
16	H-6B	#4

TRI-6342-478-0

Figure VII-1. Dolomite Compositions (from Sewards et al., 1991).

MAGNESITE

The compositions of five magnesite nodules from sample R1 were determined by EMX. The average of these compositions, normalized to 100%, is given by:

93.8% MgO 5.7% FeO 0.5% CaO

which is equivalent to the formula:

$$[Mg_{0.963}Fe_{0.033}Ca_{0.004}]CO_3$$

Similarly, the average of the compositions of 8 euhedral magnesite laths from sample R14 is given by:

88.68% MgO 10.84% FeO 0.16% CaO 0.1% MnO

which corresponds to the formula:

$$[Mg_{0.932}Fe_{0.064}Ca_{0.002}Mn_{0.002}]CO_3$$

The magnesite laths have approximately twice the iron content of the nodules; this reflects the fact that the brine from which the laths precipitated had a higher iron content than the fluid which created the secondary nodules.

CALCITE

Eight calcite analyses were obtained by EMX from sample R32. The average of these analyses yielded the following composition:

98.17% CaO 1.24% MgO 0.57% FeO

The corresponding formula is:

$$[Ca_{0.978}Mg_{0.017}Fe_{0.005}]CO_3$$

Clastic Minerals

QUARTZ

Quartz compositions from these samples were not obtained in this study.

FELDSPAR

Feldspar compositions from two samples, R8 and R35, were obtained on the electron microprobe. The average of these compositions for 13 grains on sample R8 are:

18.61% Al_2O_3 64.86% SiO_2 15.45% K_2O 0.73% Na_2O

which is equivalent to 92.5% orthoclase, 7.5% albite. The average composition of 15 feldspars on sample R35 is given by:

18.82% Al_2O_3 65.57% SiO_2 14.7% K_2O 0.73% Na_2O

which is equivalent to 93.03% orthoclase, 6.97% albite.

DETRITAL PHYLLOSILICATE GRAINS

Figures VII-2 and VII-3 are ternary plots, which show the compositions of the 4 types of phyllosilicate grains (muscovite, high and low iron chlorite, and biotite), plotted on Fe/Mg/Al and (Fe + Mg)/Al/Si axes in terms of atom %.

CLAY

Since the clay matrix that surrounds the clastic and evaporite minerals consists of four separate clay mineral phases, the composition of the matrix is highly variable. Although compositions were obtained, the results are not particularly informative since they depend on the relative proportions of the different phases. Therefore, these results are not presented here.

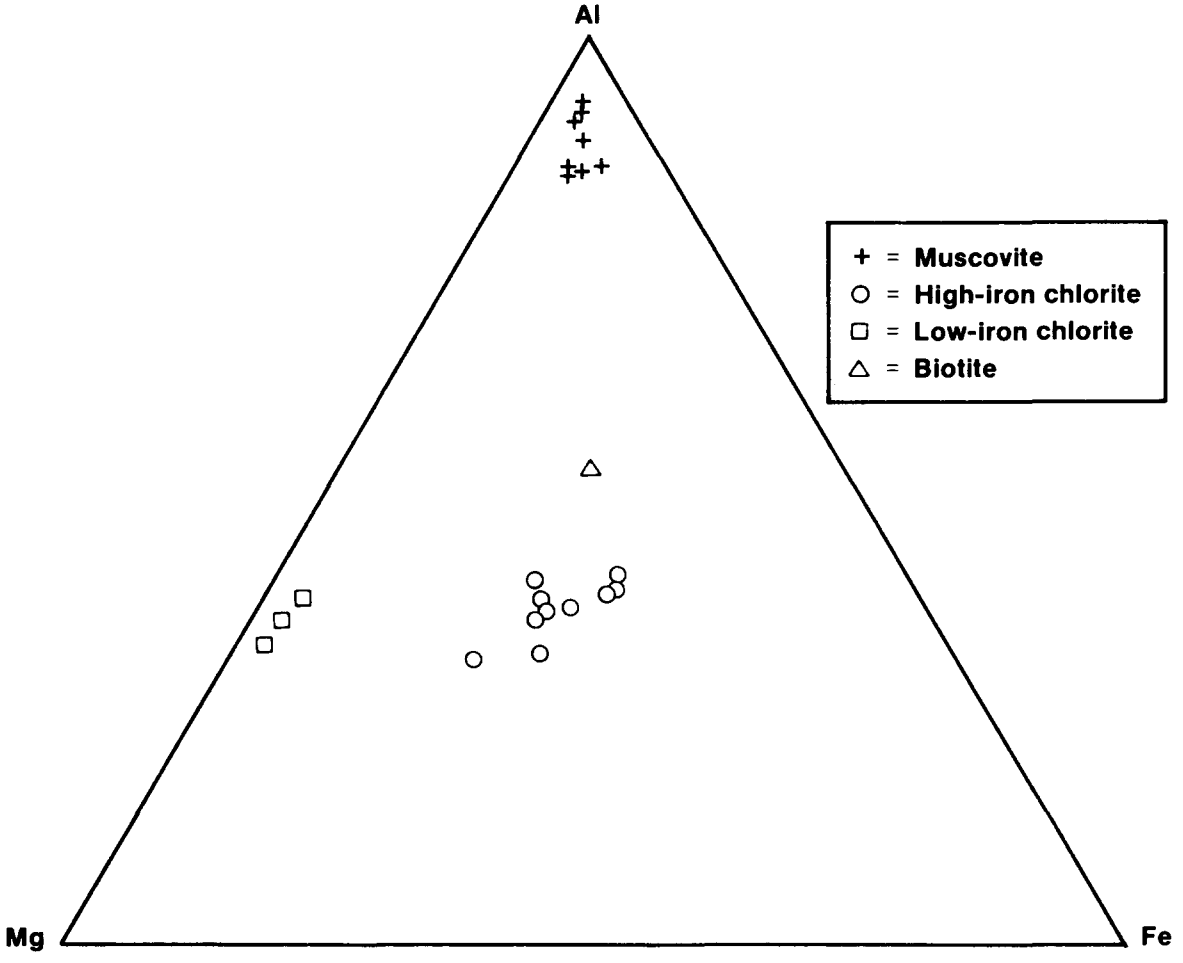

TRI-6342-479-0

Figure VII-2. Compositions of Detrital Phyllosilicate Grains in Terms of Al/Mg/Fe (Atom %).

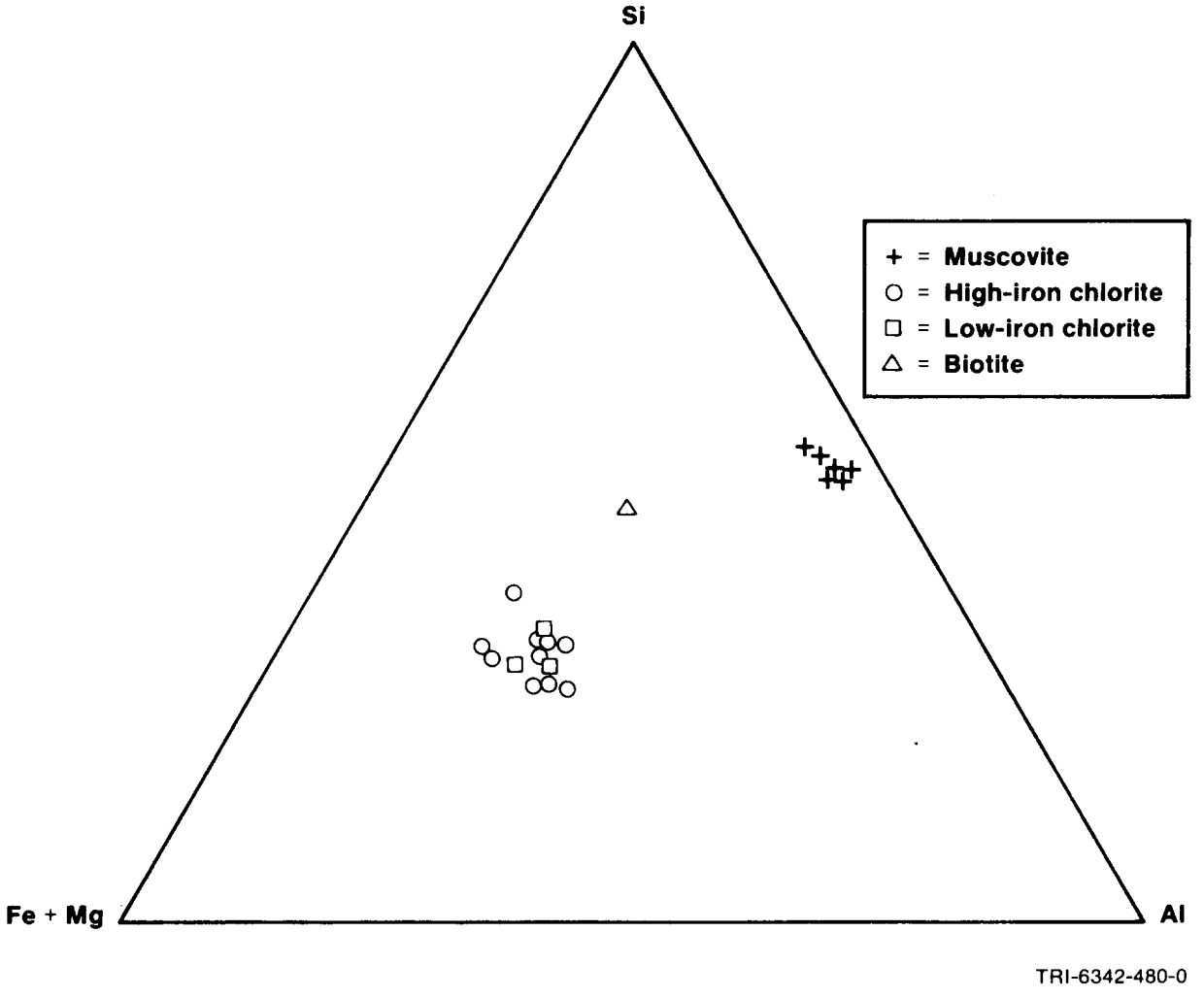

Figure VII-3. Compositions of Detrital Phyllosilicate Grains in Terms of Si/Al/Fe+Mg (Atom %).

VIII. CLAY MINERALOGY

Clay separates of 26 samples were obtained by dissolving whole rock samples in disodium ethylenediaminetetraacetic acid (EDTA) (Bodine and Fernalld, 1979) to remove carbonate and sulfate minerals, and subsequently gravity settling the residue to obtain the <2 micron fraction.

Clay Mineral Identification

Figures VIII-1 to VIII-3 show oriented mount diffractograms of 3 typical clay fractions. The results for 4 treatments: air-dried, glycolated, heated to 400°C, and heated to 550°C are displayed.

Figure VIII-1, the diffractograms for sample R8, shows the presence of 3 non-expanding clay minerals, with basal spacings of 14A, 10A, and 7A. The composition of the 10A phase was determined by analytical electron microscopy (AEM) (Sewards et al., 1991) to be dioctahedral illite. This identification was confirmed by XRD analysis of random mounts of clay separates: there is a peak at d=1.50A; this confirms the dioctahedral nature of the 10A phase. The 14A and 7A peaks have different half-widths (i.e., the 14A peak is not simply a second order diffraction of a 7A d-spacing) and clearly belong to different minerals. AEM analysis of the 7A phase shows that the mineral is serpentine (Sewards et al., 1991). The 14A phase is chlorite: samples with XRD peaks corresponding to chlorite were not analyzed by AEM, so the composition of this phase is not known. It is probably either a di/trioctahedral or a trioctahedral chlorite.

The diffractograms for sample R21 (Figure VIII-2) show the presence of minor amounts of illite and serpentine, but are dominated by a mixed-layer phase. The large peak at d=14.5A in the air-dried pattern shifts to d=15.2A upon glycolation and collapses to d=12.5A upon heating. There is also a slight bulge superimposed on the background level at d=34.8A. This is a superlattice peak of an ordered mixed-layer phase; it shifts to a slightly higher d-spacing in the glycolated pattern and collapses to a more clearly defined peak at d=22A upon heating. Reynolds (1980) shows by calculated diffractograms that this mineral is a partially ordered mixed-layer chlorite/smectite. The 400°C and 550°C patterns also reveal a distinct peak at d=14A; this peak is hidden under the broad 14.5A mixed-layer peak in the air-dried scan. The 14A peak presumably corresponds to chlorite and may either reflect packets of chlorite within the mixed-layer phase or an entirely separate phase.

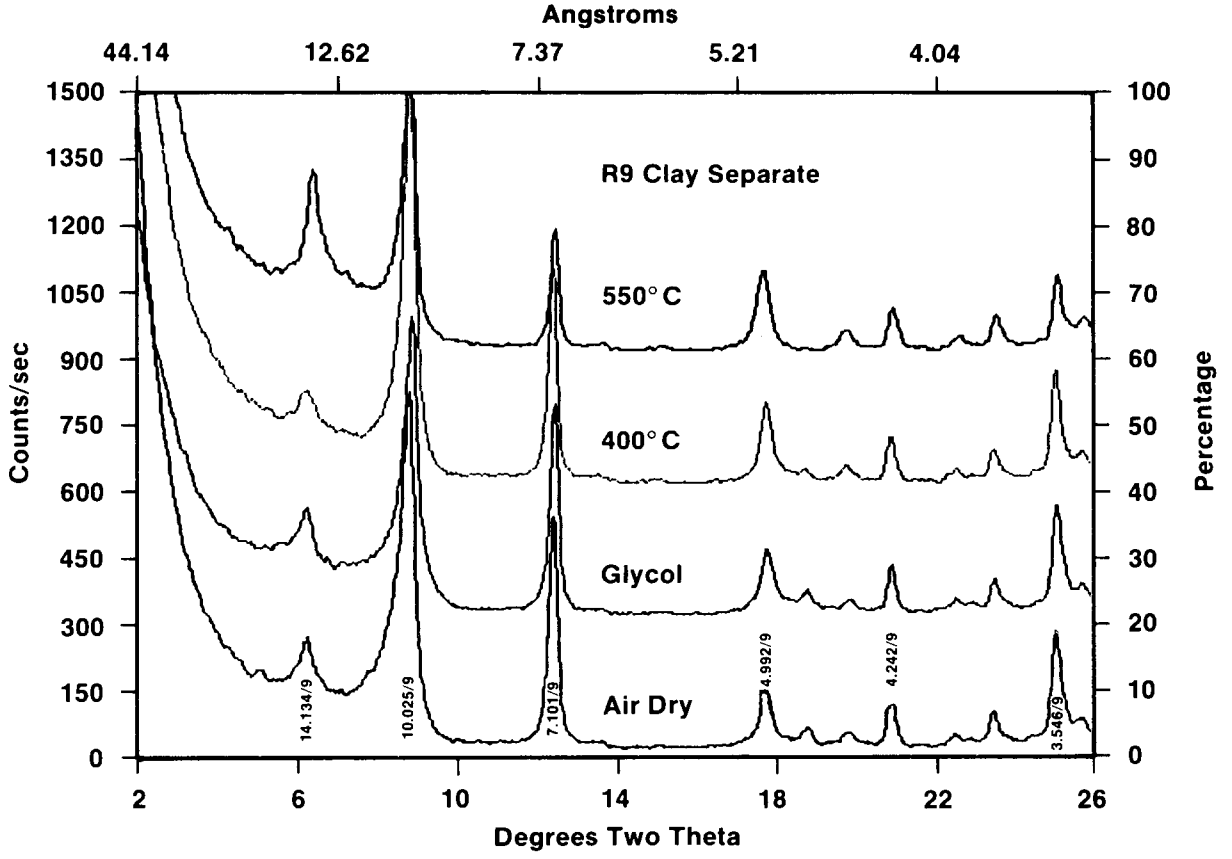

Figure VIII-1. X-Ray Diffractograms from Oriented Mounts of Clay Separate from Sample R9. Peaks represent angstroms/counts per seconds.

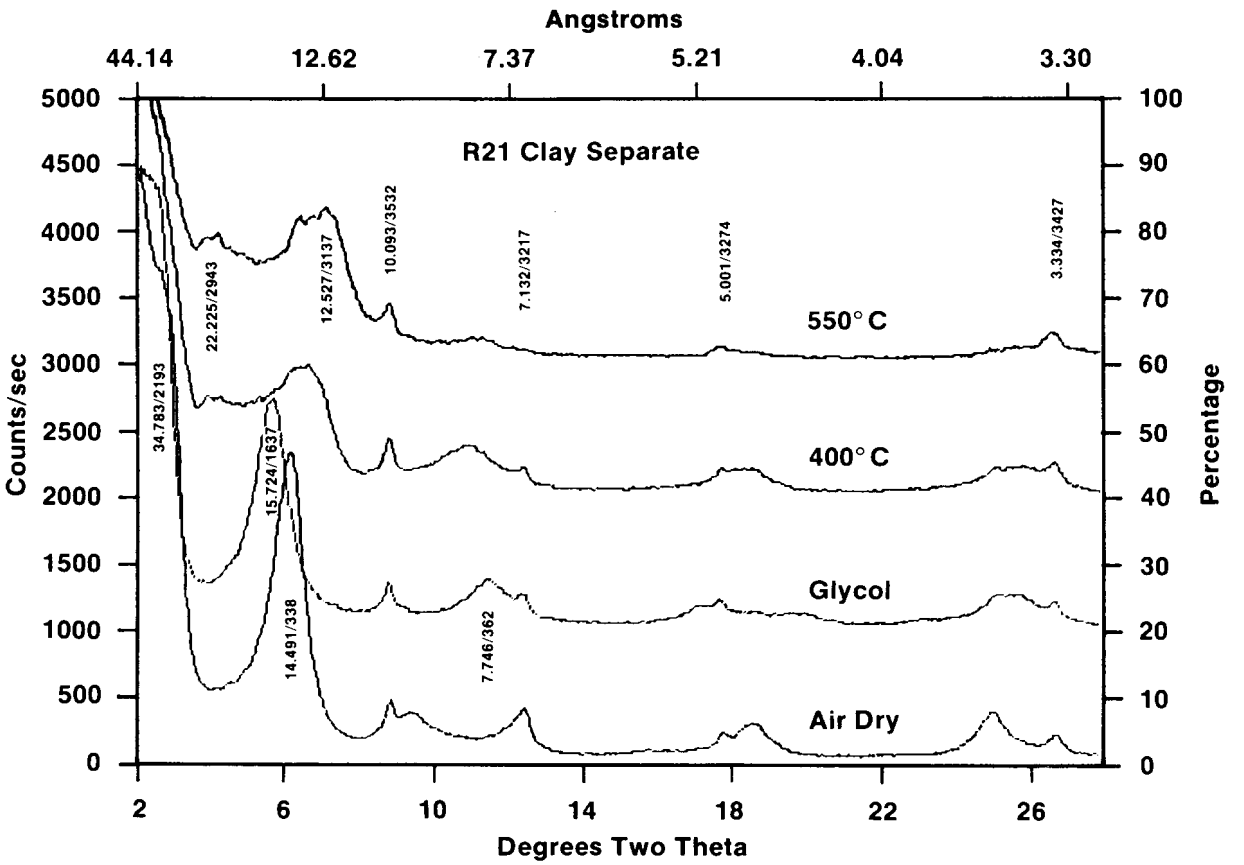

TRI-6342-482-0

Figure VIII-2. X-Ray Diffractograms from Oriented Mounts of Clay Separate from Sample R21. Peaks represent angstroms/counts per seconds.

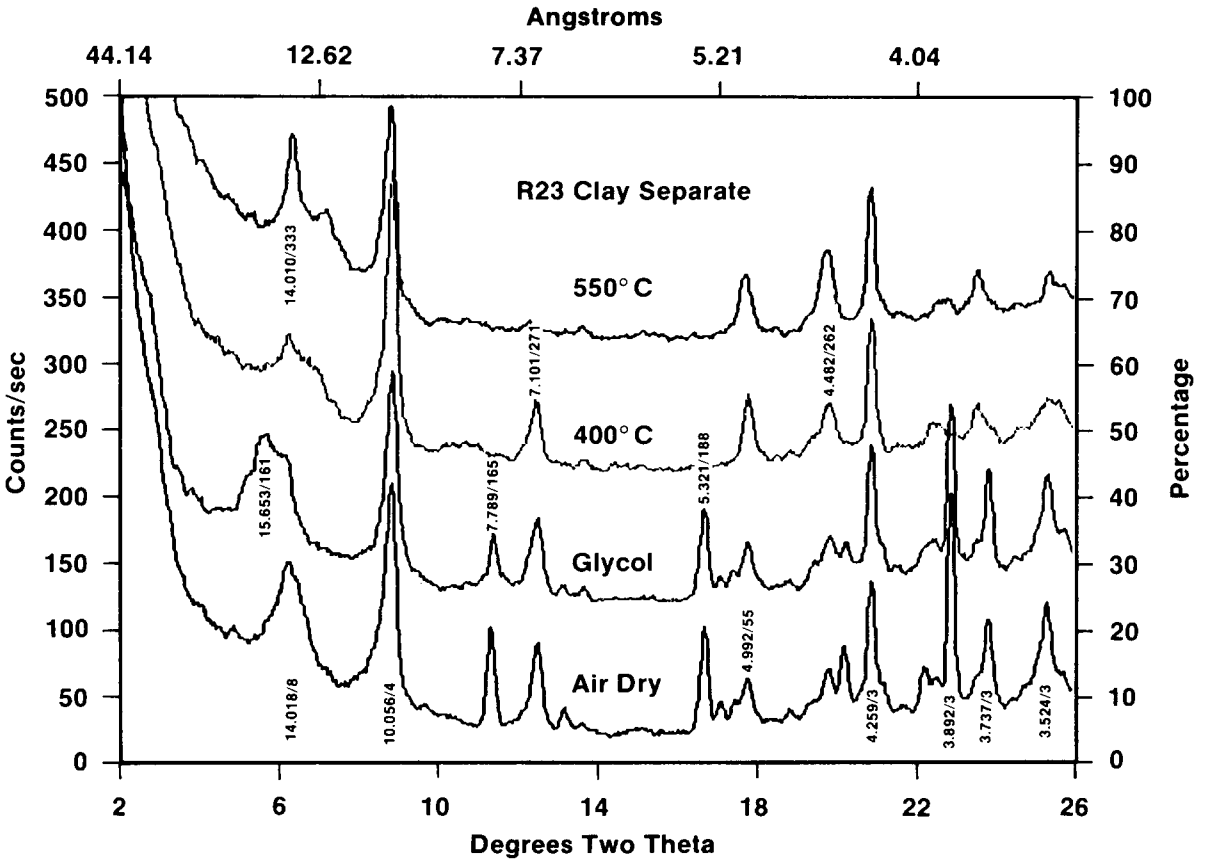

TRI-6342-481-0

Figure VIII-3. X-Ray Diffractograms from Oriented Mounts of Clay Separate from Sample R23. Peaks represent angstroms/counts per seconds.

Sample R23 (Figure VIII-3) contains illite, serpentine, chlorite, and a randomly interstratified chlorite/smectite. The peaks at d=7.79A and d=5.32A correspond to a hydroxicarbonate member of the sjögrenite family.

ILLITE

Illite is present in all samples analyzed. The diffraction maxima are sharp, indicating good crystallinity. Average crystallite thickness, determined by the Scherrer equation (Cullity, 1956) is approximately 200A (20 layers). The (001) peak at d=10A is slightly asymmetrical; this asymmetry has been attributed to the presence of interstratified smectite (Bodine, 1978). The percent interstratification was measured by Srodon's (1984) method, using the relative positions of the (002) and (003) peaks in the diffractogram of the glycolated mount, and found to be negligible.

SERPENTINE

This mineral is also present in all samples. The (001) peaks are sharp and nearly perfectly symmetrical. Average crystallite thickness is 300A, equivalent to about 43 layers. The (001) peak at d=7.1A does not vary its positions upon glycolation of the sample and is not significantly affected by the 400°C heat treatment. Heating to 550°C in some cases reduces the intensity of the peak, but never destroys it.

CHLORITE

Chlorite is present in all samples analyzed, although never in great abundance. Diffraction maxima tend to be broad, indicating poor crystallinity. Average crystallite thickness is about 80A, corresponding to six layers. The 550°C heat treatment increases the intensity of the (001) peak.

MIXED-LAYER CHLORITE/SMECTITE

This interstratified clay mineral is present in most of the samples analyzed; it is often the predominant phase. Peak widths are quite broad, which implies poor crystallinity. The percentage of chlorite in the chlorite/smectite structure was determined using the tables and calculated diffractograms compiled by Reynolds (1980): this percentage ranges from 25% to 100% (Table VIII-1). Those samples in the compositional range close to 50% chlorite show a superlattice peak at d=33A to d=34.5A (glycol); this mineral is corrensite, an ordered (R-1) mixed-layer chlorite/smectite. Samples in the range of 40% to 45% and 55% to 60% chlorite have a less distinct superlattice peak, and those samples outside the above ranges show no superlattice peak at all. This phenomenon implies that all the chlorite/smectite in these samples is at least partially ordered (Velde, 1977).

Table VIII-1. Percentage of Chlorite Layers in Mixed-Layer Chlorite/Smectite

Sample ID	% Chlorite
R1	45
R2	85
R3	65
R4	40
R5	85
R6	25
R7	100
R8	100
R9	100
R10	65
R12	100
R13	60
R14	50
R15	50
R19	50
R20	55
R22	35
R23	50
R27	35
R28	55
R29	50
R33	45
R35	50
R47	60
R48	60
R50	60

Modal Analysis

Modal mineralogical analyses were performed based on the integrated areas of diffraction maxima in the XRD patterns of glycolated samples. The calculation methods are detailed in Appendix B. Table VIII-2 lists the results of these calculations; they show that mixed-layer chlorite/smectite, illite, and serpentine are the dominant clay species, whereas chlorite never exceeds 17% of the total.

Origin of the Individual Clay Mineral Species

The clay minerals of the Rustler Formation are alteration products of detrital clay minerals, which were deposited in the Delaware Basin by the rivers that drained into the basin and, to a lesser extent, windblown ash of volcanic origin. Palmer (1981) studied Permian sediments deposited in the Palo Duro Basin and concluded that those clastic sediments were derived from granitic terrains such as the Sierra Grande uplift in central New Mexico. It is assumed here that the source for the detrital material deposited in the Delaware Basin was similar to that of the Palo Duro Basin. Clay minerals, which may be expected to form from the weathering of granitic material, include illite, dioctahedral smectite, and kaolinite; chlorite is largely unstable in most weathering profiles (Velde, 1977).

Upon deposition and burial, the clay minerals react initially with the brines at the basin floor and subsequently with the pore fluids of the sediment. If these brines and pore fluids are very magnesium-rich, it is reasonable to expect that the clay minerals will take up magnesium and lose aluminum in such an environment.

Because the interlayer space of illite is fixed with potassium ions, it is a highly stable phase, especially at low temperatures. Thus, even in an environment that is as magnesium-rich as the pore fluid of a halite-stage evaporite sediment, which is clearly out of the stability field for illite, this phase apparently does not react to any great extent with the pore fluid; the crystallites we see today are probably not very different from those deposited in Permian times.

Dioctahedral smectite, a far more reactive phase than illite, undergoes a radical transformation: magnesium substitutes for aluminum in the original smectite octahedral layers, while aluminum replaces silicon in the tetrahedral

Table VIII-2. Semi-Quantitative Clay Mineral Modal Analysis

Sample ID	Illite	Serpentine	Chlorite	C/S
R1	19	41	2	38
R2	40	32	9	19
R3	38	31	6	25
R4	39	23	11	27
R5	20	17	13	50
R6	40	45	13	2
R7	39	48	13	0
R8	47	36	17	0
R9	57	30	13	0
R10	20	12	0	68
R12	44	42	14	0
R13	7	8	0	85
R14	5	10	0	85
R15	23	11	2	64
R19	10	9	8	72
R20	6	8	3	83
R22	28	32	12	28
R23	13	7	2	78
R27	23	3	3	71
R28	12	33	3	52
R29	12	16	6	66
R33	28	35	7	30
R35	21	13	5	61
R47	13	21	12	54
R48	27	13	6	54
R50	26	16	8	50

layers; concurrently, brucitic hydroxide layers are deposited in some of the interlayer spaces. The result is a mixed-layer chlorite/smectite. The ratio of chlorite to smectite layers and the stacking sequence will determine the exact nature of the structure. It is possible that chlorite is also formed through this process. If the magnesium activity is especially high, all the interlayer spaces of the partially transformed smectite may accept brucitic hydroxide and result in a chlorite structure.

Mixed-layer illite/smectite would undergo a similar transformation: those layers not fixed by potassium (the smectite layers) would take up magnesium from the pore fluid. Some of the interlayer spaces would accept brucitic hydroxide layers, while the illite layers remain unchanged. This would result in a mixed-layer illite/smectite/chlorite. Reynolds (1980) has calculated theoretical diffraction patterns for mixed-layer illite/smectite/chlorite; these diffractograms do not differ substantially from those of mixed-layer chlorite/smectite, provided the percentage of illite layers is small.

Serpentine may be formed by direct transformation from kaolinite. Magnesium would replace aluminum in the octahedral layer, while aluminum replaces some silicon in the tetrahedral layer in order to maintain the charge balance.

Chlorite may have formed by transformation from dioctahedral smectite (see above), or it may in fact be a purely detrital phase. Detrital chlorite would presumably not react too extensively with the pore fluids in these rocks, since it is already a magnesian phase.

There are two possibilities for the mechanism of transformation from the detrital clay mineral assemblage introduced into the basin to the species we now observe. Either the original phyllosilicate lattices dissolved and reprecipitated to form the new species, or the transformations were accomplished via a layer-by-layer (solid-state) process (Bethke and Altaner, 1986; Chang et al., 1986). The presence of authigenic quartz and potassium feldspar in these samples indicates that the latter process is the more probable one: if the transformations take place layer-by-layer, both silica and aluminum are produced (Chang et al., 1986), whereas, if the dissolution mechanism occurs, silica is consumed, while aluminum is conserved. Furthermore, since these reactions took place at low temperatures, the layer-by-layer process is favored.

IX. SUMMARY AND CONCLUSIONS

We have reported here the species, quantities, distribution, and compositions of the minerals of the Rustler Formation as seen in the WIPP-19 borehole, one of the boreholes closest to the WIPP facility that was completely cored through the Rustler section. The major components, as determined by x-ray diffraction, are halite, anhydrite, gypsum, dolomite, magnesite, quartz, and clay. Minor components include calcite, pyrite, feldspar, and phyllosilicates of metamorphic origin (muscovite, biotite, and chlorite). Clay minerals, identified by XRD, include illite, serpentine, chlorite, and mixed-layer chlorite/smectite (including corrensite).

Quartz and clay, with some halite and anhydrite, dominate the lower member; the Culebra and Magenta units are primarily dolomite with some quartz and clay, while the Forty-niner Member consists of quartz, clay, and sulfates (anhydrite and gypsum).

Halite occurs in four textural styles: bedded, recrystallized halite; displacive halite; as a cement in mud/siltstones; and as a fracture filling, and is largely restricted to the lower member. Anhydrite occurs primarily as a massive, crudely banded nodular structure, although there is often evidence of partial alteration to gypsum. Gypsum also is usually massive, in a crudely banded form. The massive areas consist of fine-grained irregular crystals ("patchy" gypsum); these areas are separated by veins of "fibrous" gypsum, usually parallel to bedding. Fibrous gypsum vein filling in other lithologies is very common. Dolomite is unfossiliferous, laminated, and very fine-grained; it contains numerous vugs and fractures: these are usually lined with clay, gypsum, and powdery dolomite. Magnesite, a relatively minor component, occurs as microcrystalline nodules and as euhedral elongated platy crystals included in halite. Quartz and clay always occur together with minor amounts of feldspar and detrital phyllosilicate grains. Calcite is restricted to a thin bed above the Culebra Dolomite in the samples studied.

Halite, anhydrite, and gypsum have nearly ideal compositions, whereas dolomite has a nonideal ratio of calcium to magnesium, plus a significant amount of iron; similarly, magnesite contains some iron.

In general, this study should be considered a detailed analysis of the Rustler section mineralogy. It is unlikely that any other minerals are present in any great quantity elsewhere in the Rustler Formation. Abundances of individual minerals, however, may vary considerably in other areas of the formation.

X. REFERENCES

Bethke, C.M., and S.P. Altaner. 1986. "Layer-by-Layer Mechanism of Smectite Illitization and Application of a New Rate Law." *Clays and Clay Minerals* 34, 136-145.

Bodine, M.W. Jr. 1978. "Clay Mineral Assemblages from Drill Cores of Ochoan Evaporites, Eddy County, New Mexico" in *Geology and Mineral Deposits of Ochoan Rocks in Delaware Basin and Adjacent Areas.* New Mexico Bureau of Mines and Mineral Deposits Cir. 159. 21-31.

Bodine, M.W. Jr., and T.H. Fernalld. 1973. "EDTA Dissolution of Gypsum, Anhydrite, and Ca-Mg Carbonates." *J. Sed Petrology* 43: 1152-1156.

Borns, D.J., L.J. Barrows, D.W. Powers, and R.P. Snyder. 1983. *Deformation of Evaporites Near the Waste Isolation Pilot Plant (WIPP) Site.* Albuquerque, NM: Sandia National Laboratories.

Chang, H.K., F.T. Mackenzie, and J. Schoonmaker. 1986. "Comparisons Between the Diagenesis of Dioctahedral and Trioctahedral Smectite, Brazilian Offshore Basins." *Clays and Clay Minerals* 34: 407-423.

Cullity, B.D. 1956. *Elements of X-Ray Diffraction.* Reading, PA: Addison-Wesley.

Ferrall, C.C., and J.F. Gibbons. 1979. *Core Study of Rustler Formation Over the WIPP Site.* SAND79-7110. Albuquerque, NM: Sandia National Laboratories.

King, P.B. 1942. "Permian of West Texas and Southeastern New Mexico." *AAPG Bull.* 26: 535-763.

Hovorka, S.A. 1983. "Dissolution and Recrystallization Fabrics in Halite and the Timing of Their Development, Palo Duro Basin" in *Geology and Geohydrology of the Palo Duro Basin, Texas Panhandle.* Austin, TX: Bureau of Economic Geology.

Lambert, S.J. 1983. *Dissolution of Evaporites In and Around the Delaware Basin, Southeastern New Mexico and West Texas.* SAND82-0466. Albuquerque, NM: Sandia National Laboratories.

McGillis, K.A., and M.W. Presley. 1981. *Tansill, Salado and Alibates Formations: Upper Permian Evaporite/Carbonate Strata of the Texas Panhandle.* Austin, TX: Bureau of Economic Geology.

Palmer, D.P. 1981. "Clay Mineralogy of Permian Sabkha Sequences, Palo Duro Basin, Texas." M.S. thesis. Univeristy of Texas, Austin.

Parry, W.T., C.C. Reeves, Jr., and J.W. Leach. 1970. "Oxygen and Carbon Isotope Compositions of West Texas Lake Carbonates." *Geochim. et Cosmochim. Acta 34:* 825-830.

Reynolds, R.C. 1980. "Interstratified Clay Minerals" in: Brindley, G.W. and G. Brown, *Crystal Structures of Clay Minerals and Their X-Ray Identification.* London: p. 249-304 Mineralogical Society.

Sewards, T., M. Williams, and K. Keil. 1991. *Mineralogy of the Culebra Dolomite Member of the Rustler Formation.* SAND89-7085, Albuquerque, NM: Sandia National Laboratories.

Smith, D.B. 1971. "Possible Displacive Halite in the Permian Upper Evaporite Group of Northeast Yorkshire." *Sedimentology* 17: 221-232.

Sonnenfeld, P. 1984. *Brines and Evaporites.* Orlando, FL: Academic Press.

Stein, C.P. 1985. *Mineralogy in the Waste Isolation Pilot Plant (WIPP) Facility Stratigraphic Horizon.* SAND85-0321. Albuquerque, NM: Sandia National Laboratories.

Srodon, J. 1984. "X-Ray Powder Identification of Illitic Materials." *Clays and Clay Minerals* 32: 337-349.

Velde, B. 1977. *Clays and Clay Minerals in Natural and Synthetic Systems,* Elsevier, Amsterdam.

APPENDIX A:
ANALYTICAL PROCEDURES

X-Ray Fluorescence Spectroscopy

Whole rock samples were ground in a ballmill and/or with a mortar and pestle and passed through a 100 mesh sieve. Pressed pellets were made according to standard procedures and then analyzed on a Rigaku 3064M x-ray fluorescence (XRF) spectrometer for eight component oxides: SiO_2, Al_2O_3, CaO, MgO, FeO, Na_2O, K_2O, and SO_3. For the first seven oxides, Standard Reference Material 88b, a natural dolomitic limestone (National Bureau of Standards) was used as an analytical standard; for sulfate, sample R2, from the lower member, for which the sulfate content was determined gravimetrically, was used.

X-Ray Diffraction Analysis

Portions of the ground and sieved whole rock powders retained from the XRF pressed pellet preparation were placed in Plexiglas containers (2.5 x 2.5 x 0.4 cm), which have a 1 mm deep hollowed-out compartment. The surface of the powder was then scraped off level with the top surface of the Plexiglas container. The container was then placed in the sample holder of a Scintag PAD-V automated diffractometer and analyzed from 2° 2-θ to 60° 2-θ at a scanning rate of 3 degrees per minute using a 0.03 degree chopper increment.

Oriented mounts of the clay fractions of 26 samples were analyzed from 2° 2-θ to 30° 2-θ at a scanning rate of 3° 2-θ per minute using a 0.03 degree chopper increment.

Electron Microprobe Elemental Analysis

Polished thin sections of the samples were prepared using no water and maintaining a temperature below 60°C. The thin sections were coated with carbon in a vacuum evaporator. Mineral grains were analyzed with a JEOL 733 electron microprobe using an acceleration potential of 15KV, a beam current of 2 nanoamperes, a beam diameter of 1.5 microns, for a period of 124 seconds per analysis. Analyses were corrected according to standard Bence-Albee procedure.

Clay Fraction Separation

To obtain the clay fractions of the samples, the carbonate and sulfate minerals were dissolved using disodium ethylenediaminetetraacetic acid (EDTA). In this procedure, powdered and sieved whole rock samples were placed in a stainless steel container and boiled in a 0.25 molar disodium EDTA solution for approximately 4 hours. The fluid was then passed through a filter to separate the insoluble residue from the fluid. The residue was dried, ground and sieved, mixed with water, and left for a period of 24 hours. A portion of the dried and sieved powder was retained to obtain a random mount x-ray diffraction (XRD) pattern. The mixture was then disaggregated using a sonic dismembrator and the <2 micron fraction was separated by centrifugation. Oriented diffractometer mounts were prepared by the method of Drever (1973).

Appendix A Reference

Drever, J.I. 1973. "The Preparation of Oriented Clay Mineral Specimens for X-Ray Diffraction Analysis by a Filter-Membrane Technique." *American Mineralogist* 58: 533-554.

APPENDIX B:
MODAL MINERALOGICAL CALCULATIONS

Whole Rock Modal Analysis

Modes for the minerals identified by x-ray diffraction (XRD) were determined from the compositional data obtained by x-ray fluorescence (XRF). Based on the compositions of the individual minerals, either ideal or determined by electron microprobe analysis (EMX), a particular element, when present in only one mineral, was used to determine the mode of that mineral. For example, the only phase containing aluminum in these samples is clay, and the EMX analyses of clay aggregates show that they contain an average of 15% Al_2O_3; thus, the weight percent of clay is calculated according to the formula:

$$Clay(wt\%) = Al_2O_3 / 0.15$$

Quartz, since it contains only SiO_2, is determined by:

$$Quartz(wt\%) = SiO_2 - Clay(wt\%) \times 0.46$$

since the average SiO_2 content of the clay fraction is 46%.

The remaining mineral modes are determined using the following formulae:

$$Gypsum(wt\%) = SO_3 / 0.465$$
$$Halite(wt\%) = Na_2O / 1.886$$

$$Dolomite(wt\%) = (CaO - Gypsum(wt\%) \times 0.326) / 0.304$$

$$Anhydrite(wt\%) = SO_3/0.588$$

$$Magnesite(wt\%) = (MgO - Clay(wt\%) \times 0.135) / 0.478$$

Mineral modes determined by this method result in totals that typically lie between 90% and 100%, which suggests that the method has an accuracy of about plus or minus 10% of the amount present.

Clay Mineral Modal Analysis

Modes for the components of the clay mineral assemblages in these samples were determined by quantitative XRD analysis (Reynolds, 1985). Theoretical oriented (glycolated) diffractograms for the individual clay minerals present in the samples were calculated using the NEWMOD program. These were compared with the diffraction patterns of the glycolated mounts for the samples in this study. The following peaks were selected for quantitative analysis:

Mixed Layer Chlorite/Smectite:	d=3.46A
Chlorite (003):	d=4.73A
Illite (002):	d=5.00A
Serpentine (002):	d=3.51A

The integrated areas of the peaks in the sample diffractograms were divided by the corresponding integrated areas of the peaks in the calculated diffractograms for each mineral; the ratios were summed, and the individual ratios normalized to 100% to obtain the mode for each clay mineral.

Appendix B Reference

Reynolds, R.C. 1985. "Principles and Techniques of Quantitative Analysis of Clay Minerals by X-Ray Diffraction Methods. in *Clay Mineral Identification, a Short Course*. University of Denver. July 15, 1985.

FEDERAL AGENCIES

U. S. Department of Energy, (5)
Office of Civilian Radioactive Waste
Management
Attn: Deputy Director, RW-2
Associate Director, RW-10
Office of Program Administration
and Resources Management
Associate Director, RW-20
Office of Facilities Siting
and Development
Associate Director, RW-30
Office of Systems Integration
and Regulations
Associate Director, RW-40
Office of External Relations
and Policy
Forrestal Building
Washington, DC 20585

U. S. Department of Energy (3)
Albuquerque Operations Office
Attn: J. E. Bickel
R. Marquez, Director
Public Affairs Division
P.O. Box 5400
Albuquerque, NM 87185

U. S. Department of Energy
Attn: National Atomic Museum Library
Albuquerque Operations Office
P. O. Box 5400
Albuquerque, NM 87185

U. S. Department of Energy (4)
WIPP Project Office (Carlsbad)
Attn: Vernon Daub
J. A. Mewhinney
P.O. Box 3090
Carlsbad, NM 88221

U. S. Department of Energy
Research & Waste Management Division
Attn: Director
P. O. Box E
Oak Ridge, TN 37831

U.S. Department of Energy
Richland Operations Office
Nuclear Fuel Cycle & Production Division
Attn: R. E. Gerton
P.O. Box 500
Richland, WA 99352

U. S. Department of Energy (1)
Attn: Edward Young
Room E-178
GAO/RCED/GTN
Washington, DC 20545

U. S. Department of Energy (6)
Office of Environmental Restoration
and Waste Management
Attn: Jill Lytle, EM30
Mark Frei, EM-34 (3)
Mark Duff, EM-34
Clyde Frank, EM-50
Washington, DC 20585

U. S. Department of Energy (3)
Office of Environment, Safety and Health
Attn: Ray Pelletier, EH-231
Kathleen Taimi, EH-232
Carol Borgstrom, EH-25
Washington, DC 20585

U. S. Department of Energy
Ecological Research Division, ER-75
Office of Health and Environmental Research
Office of Energy Research
Attn: F. J. Wobber
Washington, DC 20545

U. S. Department of Energy (2)
Idaho Operations Office
Fuel Processing and Waste
Management Division
785 DOE Place
Idaho Falls, ID 83402

U.S. Department of Energy
Savannah River Operations Office
Defense Waste Processing
Facility Project Office
Attn: W. D. Pearson
P.O. Box A
Aiken, SC 29802

U. S. Department of the Interior (5)
Attn: N. Trask (MS 410)
T. Coplen (MS 431)
B. F. Jones (MS 432)
L. N. Plummer (MS 432)
I. J. Winograd (MS 432)
Geological Survey
National Center
Reston, VA 22092

U. S. Department of the Interior
Attn: J. S. McLean
Geological Survey
Box 25046, MS406
Denver, CO 80225

U. S. Department of the Interior
Attn: J. Thomas
Geological Survey
705 N. Plaza Street
Carson City, NV 89701

U. S. Department of the Interior
Attn: Librarian
National Park Service
Carlsbad Caverns National Park
3225 National Parks Highway
Carlsbad, NM 88220

U. S. Environmental Protection Agency (4)
Attn: Ray Clark (2)
Mark Cotton (2)
Office of Radiation Programs (ANR-460)
Washington, DC 20460

U.S. Geological Survey
Branch of Regional Geology
Attn: R. Snyder
MS913, Box 25046
Denver Federal Center
Denver, CO 80225

U.S. Geological Survey
Conservation Division
Attn: W. Melton
P.O. Box 1857
Roswell, NM 88201

U.S. Geological Survey (4)
Water Resources Division
Attn: Kathy Peter (2)
Roger Ferriera
Scott Anderholm
Suite 200
4501 Indian School NE
Albuquerque, NM 87110

U.S. Nuclear Regulatory Commission (8)
Attn: Joseph Bunting, HLEN 4H3 OWFN
Ron Ballard, HLGP 4H3 OWFN
Michael Bell
David Brooks
Tin Mo
Jacob Philip
John Randall
NRC Library
Mail Stop 623SS
Washington, DC 20555

Office of Nuclear Regulatory Research (4)
U. S. Nuclear Regulatory Commission
MS: NL-005
Washington, DC 20555
Attn: G. F. Birchard
L. A. Kovach
T. J. Nicholson
J. D. Randall

Boards

Defense Nuclear Facilities Safety Board
Attn: Dermot Winters
Suite 675
600 E Street, NW
Washington, DC 20004

U. S. Department of Energy
Advisory Committee on Nuclear
Facility Safety
Attn: Merritt E. Langston, AC21
Washington, DC 20585

Nuclear Waste Technical
Review Board (2)
Attn: Dr. Don A. Deere
Dr. Sidney J. S. Parry
Suite 910
1100 Wilson Blvd.
Arlington, VA 22209-2297

Richard Major
Advisory Committee on Nuclear Waste
Nuclear Regulatory Commission
7920 Norfolk Avenue
Bethesda, MD 20814

STATE AGENCIES

Environmental Evaluation Group (3)
Attn: Library
Suite F-2
7007 Wyoming Blvd., N.E.
Albuquerque, NM 87109

New Mexico Bureau of Mines
and Mineral Resources (2)
Attn: F. E. Kottolowski, Director
J. Hawley
Socorro, NM 87801

NM Department of Energy & Minerals
Attn: Librarian
2040 S. Pacheco
Santa Fe, NM 87505

NM Environmental Improvement Division
Attn: Deputy Director
1190 St. Francis Drive
Santa Fe, NM 87503

LABORATORIES/CORPORATIONS

Battelle Pacific Northwest Laboratories (7)
Attn: D. J. Bradley, K6-24
J. Relyea, H4-54
R. E. Westerman, P8-37
K. Krupa, K2-57
H. C. Burkholder, P7-41
L. Pederson, K6-47
J. Serne
Battelle Boulevard
Richland, WA 99352

Geohydrology Associates
Attn: T. E. Kelly
4015 Carlisle Blvd NE
Albquerque, NM 87110

Savannah River Laboratory (6)
Attn: N. Bibler
E. L. Albenisius
M. J. Plodinec
G. G. Wicks
C. Jantzen
J. A. Stone
Aiken, SC 29801

George Dymmel
SAIC
101 Convention Center Dr.
Las Vegas, NV 89109

INTERA Inc. (3)
Attn: G. E. Grisak
J. F. Pickens
A. Haug
Suite #300
6850 Austin Center Blvd.
Austin, TX 78731

INTERA Inc.
Attn: Wayne Stensrud
P.O. Box 2123
Carlsbad, NM 88221

INTERA Inc.
Attn: A. Marsh LaVenue
8100 Mountain Road
Suite #204D
Albuquerque, NM 87110

IT Corporation (3)
Attn: R. F. McKinney
J. Myers
R. Holt
Regional Office - Suite 700
5301 Central Avenue, NE
Albuquerque, NM 87108

IT Corporation (2)
Attn: D. E. Deal
P.O. Box 2078
Carlsbad, NM 88221

Arthur D. Little, Inc. (3)
Attn: C. R. Hadlock
Scot Foster
Philip Rury
Acorn Park
Cambridge, MA 02140-2390

Los Alamos National Laboratory (10)
Attn: A. Meijer
D. Broxton
B. Carlos
D. Eggert
D. Hobart
E. Springer
I. Triay
J. F. Kerrisk
D. T. Vaniman
K. Wolfsberg
P. O. Box 1663
Los Alamos, NM 87545

Lawrence Berkeley Laboratory (3)
Attn: F. Hale
S. L. Phillips
H. Nitsche
University of California
Berkeley, CA 94720

Martin Marietta Energy Systems, Inc.
Attn: C. S. Fore
Ecological Sciences Information Center
Oak Ridge National Laboratory - Bldg. 2001
P. O. Box X
Oak Ridge, TN 37830

Oak Ridge National Laboratory (4)
Attn: J. A. Carter
G. Jacobs
G. H. Jenks
R. Meyer
Box 2009
Oak Ridge, TN 37831

RE/SPEC, Inc.
Attn: W. Coons
P. F. Gnirk
P.O. Box 14984
Albuquerque NM 87191

RE/SPEC, Inc. (7)
Attn: L. L. Van Sambeek
G. Callahan
T. Pfeifle
J. L. Ratigan
P. O. Box 725
Rapid City, SD 57709

Center for Nuclear Waste Regulatory Analysis (6)
Attn: J. L. Russell (3)
W. Murphy
R. Pabalan
Library
Southwest Research Institute
6220 Culebra Road
San Antonio, TX 78228-0510

Environmental Engineering and Science (2)
Attn: J. O. Leckie
S. W. Park
Department of Civil Engineering
Stanford University
Stanford, CA 94305

Science Applications
International Corporation
Attn: Howard R. Pratt,
Senior Vice President
10260 Campus Point Drive
San Diego, CA 92121

Science Applications
International Corporation
Attn: Michael B. Gross
Ass't. Vice President
Suite 1250
160 Spear Street
San Francisco, CA 94105

Serata Geomechanics
Attn: Dr. Shosei Serata
4124 Lackside Drive
Richmond, CA 94806-1941

Systems, Science, and Software (2)
Attn: E. Peterson
P. Lagus
Box 1620
La Jolla, CA 92038

Westinghouse Electric Corporation (7)
Attn: Library
Lamar Trego
W. P. Poirer
W. R. Chiquelin
V. F.Likar
D. J. Moak
R. F. Kehrman
P. O. Box 2078
Carlsbad, NM 88221

Weston Corporation (1)
Attn: David Lechel
Suite 1000
5301 Central Avenue, NE
Albuquerque, NM 87108

UNIVERSITIES

Arizona State University
Attn: L. P. Knauth
Department of Geology
Tempe, AZ 85287-1404

University of Arizona
Attn: J. G. McCray
Department of Nuclear Engineering
Tucson, AZ 85721

Cornell University
Department of Physics
Attn: Dr. R. O. Pohl
Clark Hall
Ithaca, NY 14853

Florida State University (2)
Attn: J. B. Cowart
J. K. Osmond
Department of Geology
Tallahassee, FL 32308

University of Minnesota
Department of Energy and Materials Science
Attn: R. Oriani
151 Amundson Hall
421 Washington Ave SE
Minneapolis, MN 55455

University of New Mexico (3)
Geology Department
Attn: D. G. Brookins
C. J. Yapp
Library
Albuquerque, NM 87131

New Mexico Institute of Mining and Technology (3)
Attn: L. Brandvold
G. W. Gross
F. Phillips
Socorro, NM 87801

Pennsylvania State University
Materials Research Laboratory
Attn: Della Roy
University Park, PA 16802

Princeton University
Department of Civil Engineering
Attn: George Pinder
Princeton, NJ 08540

Texas A&M University
Center of Tectonophysics
College Station, TX 77840

University of Texas at Austin
Attn: Edward C. Bingler
Deputy Director
Texas Bureau of Economic Geology
Austin, TX 78712

Environmental Engineering and Science (2)
Attn: J. O. Leckie
S. W. Park
Department of Civil Engineering
Stanford University
Stanford, CA 94305

INDIVIDUALS

G. O. Bachman
4008 Hannett Avenue NE
Albuquerque, NM 87110

Carol A. Hill
Box 5444A
Route 5
Albuquerque, NM 87123

Harry Legrand
331 Yadkin Drive
Raleigh, NC 27609

Dennis W. Powers
Star Route Box 87
Anthony, TX 79821

Bob E. Watt
1447 45th St.
Los Alamos, NM 87544

LIBRARIES

Thomas Brannigan Library
Attn: Don Dresp, Head Librarian
106 W. Hadley St.
Las Cruces, NM 88001

Hobbs Public Library
Attn: Ms. Marcia Lewis, Librarian
509 N. Ship Street
Hobbs, NM 88248

New Mexico State Library
Attn: Ms. Ingrid Vollenhofer
P.O. Box 1629
Santa Fe, NM 87503

New Mexico Tech
Martin Speere Memorial Library
Campus Street
Socorro, NM 87810

Pannell Library
Attn: Ms. Ruth Hill
New Mexico Junior College
Lovington Highway
Hobbs, NM 88240

WIPP Public Reading Room
Attn: Director
Carlsbad Public Library
101 S. Halagueno St.
Carlsbad, NM 88220

Government Publications Department
General Library
University of New Mexico
Albuquerque, NM 87131

WIPP PEER PANEL

G. Ross Heath, Chairman
College of Ocean & Fishery Sciences
University of Washington
Seattle, WA 98185

Robert J. Budnitz
President, Future Resources Associates, Inc.
Suite 418
2000 Center Street
Berkeley, CA 94704

Thomas A. Cotton
4429 Butterworth Place NW
Washington, DC 20016

Patrick A. Domenico
Geology Department
Texas A&M
College Station, TX 77843-3115

Charles D. Hollister
Dean for Studies
Woods Hole Oceanographic Institute
Woods Hole, MA 02543

Thomas H. Pigford
Department of Nuclear Engineering
4153 Etcheverry Hall
University of California
Berkeley, CA 94270

Benjamin Ross
Disposal Safety Incorporated
Suite 600
1629 K Street NW
Washington, DC 20006

John Mann
Department of Geology
245 Natural History Building
1301 West Green Street
University of Illinois
Urbana, IL 61801

THE SECRETARY'S BLUE RIBBON PANEL ON WIPP

Dr. Thomas Bahr
New Mexico Water Resources Institute
New Mexico State University
Box 3167
Las Cruces, NM 88003-3167

Mr. Leonard Slosky
Slosky and Associates
Suite 1400
Bank Western Tower
1675 Tower
Denver, Colorado 80202

Mr. Newal Squyres
Eberle and Berlin
P. O. Box 1368
Boise, Idaho 83701

Dr. Arthur Kubo
Vice President
BDM International, Inc.
7915 Jones Branch Drive
McLean, VA 22102

Mr. Robert Bishop
Nuclear Management Resources Council
Suite 300
1776 I Street, NW
Washington, DC 20006-2496

NATIONAL ACADEMY OF SCIENCES, WIPP PANEL

Dr. Charles Fairhurst, Chairman
Department of Civil and
Mineral Engineering
University of Minnesota
500 Pillsbury Dr. SE
Minneapolis, MN 55455

Dr. John O. Blomeke
Route 3
Sandy Shore Drive
Lenoir City, TN 37771

Dr. John D. Bredehoeft
Western Region Hydrologist
Water Resources Division
U.S. Geological Survey (M/S 439)
345 Middlefield Road
Menlo Park, CA 94025

Dr. Karl P. Cohen
928 N. California Avenue
Palo Alto, CA 94303

Dr. Fred M. Ernsberger
250 Old Mill Road
Pittsburgh, PA 15238

Dr. Rodney C. Ewing
Department of Geology
University of New Mexico
200 Yale, NE
Albuquerque, NM 87131

B. John Garrick
Pickard, Lowe & Garrick, Inc.
2260 University Drive
Newport Beach, CA 92660

John W. Healy
51 Grand Canyon Drive
Los Alamos, NM 87544

Leonard F. Konikow
U.S. Geological Survey
431 National Center
Reston, VA 22092

Jeremiah O'Driscoll
505 Valley Hill Drive
Atlanta, GA 30350

Dr. D'Arcy A. Shock
233 Virginia
Ponca City, OK 74601

Dr. Christopher G. Whipple
Electric Power Research Institute
3412 Hillview Avenue
Palo Alto, CA 94303

Dr. Peter B. Myers, Staff
Director
National Academy of Sciences
Committee on Radioactive
Waste Management
2101 Constitution Avenue
Washington, DC 20418

Dr. Geraldine Grube
Board on Radioactive
Waste Management
GF462
2101 Constitution Avenue
Washington, DC 20418

Dr. Ina Alterman
Board on Radioactive Waste
Management
GF462
2101 Constitution Avenue
Washington, DC 20418

FOREIGN ADDRESSES

Studiecentrum Voor Kernenergie
Centre D'Energie Nucleaire
Attn: Mr. A. Bonne
SCK/CEN
Boeretang 200
B-2400 Mol
BELGIUM

Atomic Energy of Canada, Ltd. (2)
Whiteshell Research Estab.
Attn: Peter Haywood
John Tait
Pinewa, Manitoba, CANADA
R0E 1L0

Dr. D. K. Mukerjee
Ontario Hydro Research Lab
800 Kipling Avenue
Toronto, Ontario, CANADA
M8Z 5S4

Department of Earth Sciences and
Quaternary Sciences Institute
Attn: T. W. D. Edwards
University of Waterloo
Waterloo, Ontario
CANADA N2L 3Gl

Mr. Francois Chenevier, Director (2)
ANDRA
Route du Panorama Robert Schumann
B.P.38
92266 Fontenay-aux-Roses Cedex
FRANCE

Mr. Jean-Pierre Olivier
OECD Nuclear Energy Agency
Division of Radiation Protection
and Waste Management
38, Boulevard Suchet
75016 Paris, FRANCE

Claude Sombret
Centre D'Etudes Nucleaires
De La Vallee Rhone
CEN/VALRHO
S.D.H.A. BP 171
30205 Bagnols-Sur-Ceze
FRANCE

Bundesministerium fur Forschung und
Technologie
Postfach 200 706
5300 Bonn 2
FEDERAL REPUBLIC OF GERMANY

Bundesanstalt fur Geowissenschaften
und Rohstoffe
Attn: Michael Langer
Postfach 510 153
3000 Hannover 51
FEDERAL REPUBLIC OF GERMANY

Hahn-Meitner-Institut fur Kernforschung
Attn: Werner Lutze
Glienicker Strasse 100
100 Berlin 39
FEDERAL REPUBLIC OF GERMANY

Institut fur Tieflagerung (4)
Attn: K. Kuhn
Theodor-Heuss-Strasse 4
D-3300 Braunschweig
FEDERAL REPUPLIC OF GERMANY

Kernforschug Karlsruhe
Attn: K. D. Closs
Postfach 3640
7500 Karlsruhe
FEDERAL REPUBLIC OF GERMANY

Physikalisch-Technische Bundesanstalt
Attn: Peter Brenneke
Postfach 33 45
D-3300 Braunschweig
FEDERAL REPUBLIC OF GERMANY

Hermann Gies
Institut fur Tieflagerung, Gruppe Geochemie
Gesellschaft fur Strahlen und Umweltforschung mbH
Theodor-Heuss-Strasse 4
D-3300 Braunschweig
FEDERAL REPUBLIC OF GERMANY

British Geological Survey (3)
Hydrogeology Group
Attn: G. Darling
R. A. Downing
R. L. F. Kay
Maclean Building
Crowmarsh Gifford
Wallingford
Oxfordshire OX10 8BB
GREAT BRITAIN

U. K. Atomic Energy Authority (3)
Attn: M. Ivanovich
R. Otlet
A. J. Walker
Centre for Nuclear Applications
Isotope Measurement Laboratory
Harwell
Oxfordshire OX11 ORA
GREAT BRITAIN

D. R. Knowles
British Nuclear Fuels, plc
Risley, Warrington, Cheshire WA3 6AS
1002607 GREAT BRITAIN

Shingo Tashiro
Japan Atomic Energy Research Institute
Tokai-Mura, Ibaraki-Ken
319-11 JAPAN

Netherlands Energy Research Foundation
ECN (2)
Attn: Tuen Deboer, Mgr.
L. H. Vons
3 Westerduinweg
P.O. Box 1
1755 ZG Petten, THE NETHERLANDS

Svensk Karnbransleforsorjning AB
Attn: Fred Karlsson
Project KBS
Karnbranslesakerhet
Box 5864
10248 Stockholm, SWEDEN

SANDIA INTERNAL

400 L. D. Tyler
1510 J. C. Cummings
1512 K. L. Erickson
1520 C. W. Peterson
1521 J. G. Arguello
1521 H. S. Morgan
3141 S. A. Landenberger (5)
3151 Supervisor (3)
3154-1 C. L. Ward, (10) for DOE/OSTI
6000 V. L. Dugan, Acting
6230 R. K. Traeger
6232 W. R. Wawersik
6233 D. J. Borns
6233 J. C. Eichelberger
6233 J. L. Krumhansl
6233 S. J. Lambert
6233 C. L. Stein
6300 T. O. Hunter, Acting
6310 T. E. Blejwas, Acting
6313 L. E. Shephard
6315 F. B. Nimick, Acting
6315 R. J. Glass
6315 M. D. Siegel (5)
6340 W. D. Weart
6340A A. R. Lappin
6340 S. Y. Pickering
6341 R. C. Lincoln
6341 Staff (9)
6341 Sandia WIPP Central Files (10)

6342 D. R. Anderson
6342 Staff (11)
6343 T. M. Schultheis
6343 Staff (2)
6344 E. Gorham
6344 Staff (10)
6345 B. M. Butcher, Acting
6345 Staff (9)
6346 J. R. Tillerson
6346 Staff (7)
8524 J. A. Wackerly (SNLL Library)
9300 J. E. Powell
9310 J. D. Plimpton
9320 M. J. Navratil
9325 L. J. Keck (2)
9330 J. D. Kennedy
9333 O. Burchett
9333 J. W. Mercer
9334 P. D. Seward

*U.S. GOVERNMENT PRINTING OFFICE 1991-0-573-038/44021